

# Structural Shape Estimation Using Shaped Sensors

Mark Sven-Erik Andersson  
Edward F. Crawley

May 1996

SERC #1-96-R

(Under the sponsorship of AFOSR and SERC)

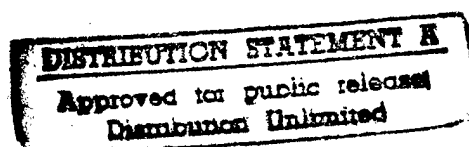
20 Dec 96

Rec'd

10894-11-20 rec'd

on 20 Dec 96

(by S. Kim  
on 23 Dec 96)



This is the final report for Air Force Office of Scientific Research Grant F49620-94-1-0160.

19971003 022

DTIC QUALITY INSPECTED 8

REPORT DOCUMENTATION PAGE			Form Approved OMB No. 0704-0188	
Public reporting burden for this collection of information is estimated to average 1 hour per response, including the time for reviewing instructions, searching existing data sources, gathering and maintaining the data needed, and completing and reviewing the collection of information. Send comments regarding this burden estimate or any other aspect of this collection of information, including suggestions for reducing this burden, to Washington Headquarters Services, Directorate for Information Operations and Reports, 1215 Jefferson Davis Highway, Suite 1204, Arlington, VA 22202-4302, and to the Office of Management and Budget, Paperwork Reduction Project (0704-0188), Washington, DC 20503.				
1. AGENCY USE ONLY (Leave blank)		2. REPORT DATE 12/20/96	3. REPORT TYPE AND DATES COVERED Final 2/1/94 - 7/31/96	
4. TITLE AND SUBTITLE Actuator-Sensor-Controller Optimization for Intelligent Dynamic Structures			5. FUNDING NUMBERS	
6. AUTHOR(S) Mark Sven-Erik Anderson and Edward F. Crawley				
7. PERFORMING ORGANIZATION NAME(S) AND ADDRESS(ES) Dept of Aeronautical & Astronautical Engineering MIT 77 Massachusetts Ave Cambridge, MA 02139			8. PERFORMING ORGANIZATION REPORT NUMBER AFOSR-TR-97 0354	
9. SPONSORING/MONITORING AGENCY NAME(S) AND ADDRESS(ES) AFOSR 110 Duncan Avenue, Suite B115 Bolling AFB, DC 20332-8080			10. SPONSORING/MONITORING AGENCY REPORT NUMBER F49620-94-1-0160	
11. SUPPLEMENTARY NOTES				
12a. DISTRIBUTION / AVAILABILITY STATEMENT  Approved for public release; distribution unlimited.			12b. DISTRIBUTION CODE  Approved for public Release Distribution unlimited	
13. ABSTRACT The estimation of the global shape of intelligent structures using an array of shaped sensors is investigated. The design of these sensors and their functional requirements are discussed. It is found that certain spatially averaging strain sensors can be used to satisfy these requirements. The output and transfer function characteristics of spatially averaging sensors with arbitrary spatial weightings are given for a sinusoidal and exponential strain fields. desirable spatial weightings are then identified. A number of integration schemes used to process sensor measurements and estimate global shape are described. These schemes are then used with spatially averaging sensors to estimate the shape of pinned-pinned and clamped-free beams. Evanescent components in the modeshapes of the clamped-free beam make it more difficult to estimate the shape at low frequencies while ensuring reduced observability of the sensors to higher order modes. A measurement near the root is determined to be important, as is the use of shaped sensors. Finally, an experiment using a clamped-free beam fitted with a number of point and shaped strain sensors was conducted to verify that accurate modeshape estimation can be performed.				
14. SUBJECT TERMS Intelligent structures, modeshape sensors, spatially averaging, shaped sensors			15. NUMBER OF PAGES 75	
			16. PRICE CODE	
17. SECURITY CLASSIFICATION OF REPORT unclassified	18. SECURITY CLASSIFICATION OF THIS PAGE unclassified	19. SECURITY CLASSIFICATION OF ABSTRACT unclassified	20. LIMITATION OF ABSTRACT unlimited	

---

# Abstract

---

The estimation of the global shape of intelligent structures using an array of shaped sensors is investigated. The design of these sensors and their functional requirements are discussed. It is found that certain spatially averaging strain sensors can be used to satisfy these requirements.

The output and transfer function characteristics of spatially averaging sensors with arbitrary spatial weightings are given for a sinusoidal and exponential strain fields. Desirable spatial weightings are then identified.

A number of integration schemes used to process sensor measurements and estimate global shape are described. These schemes are then used with spatially averaging sensors to estimate the shape of pinned-pinned and clamped-free beams. Evanescent components in the modeshapes of the clamped-free beam make it more difficult to estimate the shape at low frequencies while ensuring reduced observability of the sensors to higher order modes. A measurement near the root is determined to be important, as is the use of shaped sensors.

Finally, an experiment using a clamped-free beam fitted with a number of point and shaped strain sensors was conducted to verify that accurate modeshape estimation can be performed.

---

---

# Contents

---

---

<b>1</b>	<b>Introduction</b>	<b>15</b>
<b>2</b>	<b>Shaped Sensors</b>	<b>19</b>
2.1	Shaped Sensor Definition . . . . .	19
2.2	Sensor Outputs . . . . .	21
<b>3</b>	<b>Shape Estimation Schemes</b>	<b>27</b>
3.1	Trapezoidal Integration . . . . .	27
3.2	Simpson's Rule . . . . .	28
3.3	Modeshape Fitting . . . . .	28
3.4	Kalman Filter . . . . .	32
3.5	Boundary Problems . . . . .	33
<b>4</b>	<b>Shape Estimation of a Pinned-Pinned Beam</b>	<b>35</b>
4.1	Description . . . . .	35
4.2	Trapezoidal Rule . . . . .	37
4.3	Simpson's Rule . . . . .	39
4.4	GDSF Scheme . . . . .	40
4.5	LSGDSF Scheme . . . . .	41
4.6	Summary . . . . .	42
<b>5</b>	<b>Shape Estimation of a Clamped-Free Beam</b>	<b>45</b>
5.1	Description . . . . .	45

---

5.2	Trapezoidal Rule . . . . .	47
5.3	Simpson's Rule . . . . .	49
5.4	GDSF Scheme . . . . .	51
5.5	LSGDSF Scheme . . . . .	54
5.6	Summary . . . . .	55
<b>6</b>	<b>Experimental Shape Estimation Results</b>	<b>59</b>
6.1	Description . . . . .	59
6.2	Trapezoidal Rule . . . . .	62
6.3	Simpson's Rule . . . . .	64
6.4	GDSF Scheme . . . . .	66
6.5	LSGDSF Scheme . . . . .	69
6.6	Summary . . . . .	71
<b>7</b>	<b>Conclusions</b>	<b>73</b>
	<b>References</b>	<b>77</b>

---

# List of Figures

---

2.1	Transfer functions of rectangular and triangular sensors, including asymptotic behavior at high frequency. . . . .	24
4.1	Estimate of the tip slope response given a tip moment disturbance, using point and triangular sensors with the trapezoidal rule. . . . .	38
4.2	Estimate of the tip slope response given a tip moment disturbance, using point and triangular sensors with the trapezoidal rule. . . . .	39
4.3	Estimate of the tip slope response given a tip moment disturbance, using point and triangular sensors with the GDSF scheme. . . . .	40
4.4	Estimate of the tip slope response given a tip moment disturbance, using point and triangular sensors with the LSGDSF scheme when fitting four shape functions. . . . .	42
5.1	Estimate of the tip deflection response given a tip force disturbance, using an array of seven point and Triangular sensors with the trapezoidal rule. . . . .	48
5.2	Estimate of the tip deflection response given a tip force disturbance, using an array of eight point and Triangular sensors with the trapezoidal rule. . . . .	49
5.3	Estimate of the tip deflection response given a tip force disturbance, using point and Triangular sensors with Simpson's rule. . . . .	50
5.4	Estimate of the tip deflection response given a tip force disturbance, using point and Triangular sensors with the Simpson's rule. . . . .	51
5.5	Estimate of the tip deflection response given a tip force disturbance, using point and triangular sensors with the GDSF rule. . . . .	52
5.6	Estimate of the tip deflection response given a tip force disturbance, using point and triangular sensors with the GDSF rule. . . . .	53

5.7	Estimate of the tip deflection response given a tip force disturbance, using point and triangular sensors with the LSGDSF rule. . . . .	54
5.8	Estimate of the tip deflection response given a tip force disturbance, using point and triangular sensors with the LSGDSF rule. . . . .	56
6.1	Perspective view of T-Section beam with arrangement of array of 22 Bartlett sensors. . . . .	60
6.2	T-Section beam with arrangement of array of 22 Bartlett sensors on the top surface and seven point sensors on the bottom surface of the central flange. . . . .	60
6.3	Comparison of transfer functions of a finite element model, from tip force to exact tip displacement and tip displacement response estimated from simulated sensor outputs using the trapezoidal rule. . . .	63
6.4	Comparison of experimentally measured transfer functions from tip force to actual tip displacement and tip displacement response estimated by numerically integrating measured sensor transfer functions using the trapezoidal rule. . . . .	64
6.5	Comparison of transfer functions of a finite element model, from tip force to exact tip displacement and tip displacement response estimated from simulated sensor outputs using Simpson's rule. . . . .	65
6.6	Comparison of experimentally measured transfer functions from tip force to actual tip displacement and tip displacement response estimated by numerically integrating measured sensor transfer functions using Simpson's rule. . . . .	66
6.7	Comparison of transfer functions of a finite element model, from tip force to exact tip displacement and tip displacement response estimated from simulated sensor outputs using the GDSF scheme. . . . .	67
6.8	Comparison of experimentally measured transfer functions from tip force to actual tip displacement and tip displacement response estimated by numerically integrating measured sensor transfer functions using the GDSF scheme. . . . .	68
6.9	Comparison of transfer functions of a finite element model, from tip force to exact tip displacement and tip displacement response estimated from simulated sensor outputs using the LSGDSF-4 rule. . . .	69

6.10 Comparison of experimentally measured transfer functions from tip force to actual tip displacement and tip displacement response estimated by numerically integrating measured sensor transfer functions using the LSGDSF-4 rule. . . . .	70
--	----



---

---

# List of Tables

---

---

2.1	Rolloff properties of the sensor transfer function $\mathcal{T}(k)$ for a sensor weighting $f(x)$ possessing continuous derivatives over its entire length.	23
2.2	Properties of shaped sensors with selected weightings. . . . .	25
4.1	Estimation errors of various integration schemes in estimating the response of the tip slope of a pinned-pinned beam. . . . .	36
5.1	Estimation errors of various integration schemes in estimating the response of the tip displacement of a clamped-free beam. . . . .	46

## CHAPTER 1

---

# Introduction

---

The motivation for this work is to determine methods to use available sensor outputs to estimate a performance variable which cannot be measured directly. For the purposes of this work, assume that the performance variable is either an absolute displacement or a relative displacement between widely spaced parts of the structure.

Since such displacements are typically difficult to measure in practice, the objective is to determine the how to infer the displacements using curvature measurements over the structure. Using a numerical integration rule, a shape fitting scheme or a temporal estimation scheme, this can be accomplished. Beam-like structures are considered in this work, and the curvature measurements are made by spatially weighted strain sensors. Such sensors are used to introduce rolloff to the higher modes of the structure.

Many other researchers have investigated the use of distributed sensors and actuators for the development and control of intelligent structures. Such structures typically have a large number of sensors and actuators distributed over their area[14].

For example, Lee and Moon[10, 11, 12, 9] have worked on a variety of topics concerning distributed sensors and actuators. They have developed theoretical results

for distributed sensing and actuation, have implemented modal control on a plate using modal sensors and actuators, and have created distributed sensors to make measurements of the bending and torsion of a plate.

Burke and Hubbard have also done much work on distributed sensors and actuators, including the use of a single distributed actuators to add damping to all the modes of a pinned-pinned beam[4]. The concept of collocation of distributed transducers was discussed by Burke who showed that to be collocated, the spatial apertures of the sensor and actuator have to be equal, as do their spatial derivative orders[5]. The general mathematical modeling of one-dimensional and two-dimensional distributed transducers of was introduced by Burke, Sullivan and Hubbard[3, 13], using Macauley notation and the theory of multivariate distributions.

Previous work concentrating on the use of distributed sensors for intelligent structures was done by Andersson and Crawley[1, 2]. The analytical behavior and properties of one-dimensional sensors was derived for arbitrary spatial weightings. It was shown how this weighting affects the eventual rolloff rate of the sensor, and how an array of them might be used to infer the global shape of a one-dimensional structure.

For the purposes of this work, the approach taken is to first formulate the functional requirements for a system of sensors used to estimate the global shape of a structure. Then, we present a summary of the basic spatial weightings considered for shaped sensors and to show their frequency properties. The next step is to introduce schemes to estimate the global shape of a structure using curvature measurements made by an array of shaped sensors. Numerical results obtained using such schemes are then presented for a pinned-pinned beam supporting purely sinusoidal modeshapes, and for a clamped-free beam supporting modeshapes with sinusoidal and exponential evanescent components. It is illustrated how shape estimation for the

---

latter system is much more difficult due to the presence of the exponential mode-shape components at the boundaries. Finally, experimental results using a beam fitted with an array of triangular (Bartlett) and point strain sensors are presented, and conclusions are drawn.

We now discuss the functional requirements for a sensor system in global shape estimation. These requirements can be thought of as those which relate to single sensors, those dealing with the system as a whole, and those that involve practical implementation issues.

The functional requirements that relate to individual sensors are: they must be able to accurately observe modes targeted for control; their observability to higher order modes should roll off quickly; this rolloff should not be accompanied by uncertainties in the sign of the output.

The sensor system as a whole should be able to accurately resolve the shape of modes targeted for control, offer reduced observability of modes beyond the targeted bandwidth.

Practical implementation requirements are simply that the sensors be of finite length, that regions of negative weighting should be avoided as they complicate fabrication, and that sensors placed near structural boundaries be truncated in a fashion that minimizes their performance degradation.

It is the objective of this work to develop a system of sensors that meets, to the extent possible, these functional requirements.

## CHAPTER 2

---

# Shaped Sensors

---

## 2.1 Shaped Sensor Definition

To begin we investigate the behavior of single spatially averaging sensors. A variety of signals can be measured using such sensors and therefore, they can be used in a number of different structural sensing applications. For the purposes of this work, however, it will be assumed that the shaped sensors report measurements of spatially averaged extensional strain signals. We now derive the response of these sensors to strain fields that are spatially sinusoidal or exponential, since such fields can be used to express modeshapes of beam-like structures. Expressions are given for the transfer function of nontruncated sensors whose weighting is continuous over its length. Expressions for the transfer function of sensors incorporating a derivative discontinuity, or whose weighting is partially truncated at a structure boundary have also been derived in detail[2].

In the design of shaped sensors, the most important characteristic is their spatial weighting. It is this weighting that controls how the magnitude and phase of the sensor output vary with changes in the spatial nature of the strain field. Let  $f(x)$  define the

spatial weighting of a sensor, and let this weighting be nonzero over a finite region  $[-l/2, l/2]$  of the structure. The sensor output is then a filtered measurement of the longitudinal strain of the form

$$y(t) = \int_{-l/2}^{l/2} f(x) \epsilon(x, t) dx \quad (2.1)$$

where  $\epsilon(x, t)$  is the longitudinal strain present in the structure and  $l$  is the length of the sensor. The weighting function  $f(x)$  is essentially the spatial sensitivity of the sensor. Depending on the device or material used as the sensor, this might be done by (a) varying the width of the sensor; (b) varying the thickness of the sensor; (c) segmenting the sensor and forming a weighted sum of the measurements of different sensor segments in a signal processing system; (d) or by varying the distance of the sensor from the elastic axis of a beam in bending. Note that the weighting functions of multiple sensors should be scaled such that  $\int_{-l/2}^{l/2} f(x) dx$  is the same for all of them. This will then ensure that all the sensors will have the same output when measuring the same uniform strain.

As an example of a physical implementation, the sensor might be made of a piece of thin Polyvinylidene Fluoride (PVDF) piezoelectric film bonded to the surface of a beam[6]. The weighting function  $f(x)$  is easily implemented by spatially varying the width of one or both of the electrodes on the film or by cutting the film to the desired width. The output of the PVDF sensor is a charge proportional to a filtered measurement of the surface strain. The magnitude of this charge depends on the area of the electrode. Therefore, the gain of the sensor can be varied spatially by spatially varying the electrode area. The charge generated by the sensor is given by

$$Q(t) = d_{31} E_p \int_{-l/2}^{l/2} f(x) \epsilon(x, t) dx \quad (2.2)$$

where  $E_p$  is Young's modulus for the piezoelectric film,  $f(x)$  is the width of the sensor electrode,  $\epsilon(x, t)$  is the surface longitudinal strain, and  $d_{31}$  is a piezoelectric constant with units of charge per unit area per unit stress. This constant relates mechanical stress to electric displacement.

## 2.2 Sensor Outputs

The design of shaped sensors is related to the design of temporal windowing filters through a straight-forward transformation from the temporal to the spatial (wavenumber) domain. Due to the similarity of shaped sensors and temporal windowing functions, some of their design techniques can be extended to applications involving shaped sensors. As with temporal windows, the spatial weighting of the sensor is changed to tailor the magnitude response of the sensor. Further, the effective sensor length can be changed to control the spatial frequency at which magnitude rolloff commences. In certain circumstances, shaped sensors can exhibit magnitude rolloff without any more phase lag than a point sensor located at the center of the sensor. We now derive the output and transfer function of a shaped sensor in a spatially sinusoidal strain field. The transfer function of a shaped sensor is defined here as the ratio of the output of the shaped sensor to the output of a point sensor located at its center. Note that this is not really a transfer function describing a dynamic process and so is not subject to Bode's gain-phase theorem.

Let the spatial weighting of the sensor be  $f(x - x_0)$ , and be centered at  $x = x_0$ . Assuming that the weighting function  $f(x - x_0)$  is non-zero only over the closed interval  $[-l/2 + x_0, l/2 + x_0]$ , its output as a function of the spatial frequency  $k$  of

the strain field is given by

$$y(k) = \int_{-l/2+x_0}^{l/2+x_0} f(x-x_0) \sin(kx) dx \quad (2.3)$$

By repeatedly integrating this expression by parts, an infinite series solution for the output of the sensor can be found. To obtain the sensor transfer function, the sensor output must be divided by the strain at the center of the sensor,  $\sin(kx_0)$ . By expanding the sine and cosine terms and assuming the weighting is symmetric and continuous, the transfer function becomes[2]

$$\begin{aligned} T(k) = \sum_{i=0}^{\infty} \left\{ \frac{2(-1)^i}{k^{(2i+1)}} f^{(2i)}(l/2) \sin(kl/2) \right. \\ \left. + \frac{2(-1)^i}{k^{(2i+2)}} f^{(2i+1)}(l/2) \cos(kl/2) \right\} \end{aligned} \quad (2.4)$$

It can be seen that the first term in the series of Equation (2.4) rolls off at  $1/k$ . This is the only term remaining for a rectangular weighting, which has  $f(\pm l/2) \neq 0$  and  $f^{(i)} = 0 (i > 0)$ . The resulting transfer function is the well-known Sinc function,  $\sin(\alpha k)/\alpha k$ .

By making the weighting go to zero at the ends points by setting  $f(\pm l/2) = 0$ , the first term can be eliminated and the asymptotic rolloff is increased to  $1/k^2$ . By making the end points of the weighting  $f(x)$  more smooth, by making higher and higher derivatives,  $f'(x)$ ,  $f''(x)$ , etc., zero, we can increase the rolloff rate further. This behavior is shown in Table 2.1.

For a sensor in an exponential strain field, its output is given by

$$y(k) = \int_{-l/2+x_0}^{l/2+x_0} f(x-x_0) e^{-kx} dx \quad (2.5)$$



**Table 2.1:** Rolloff properties of the sensor transfer function  $T(k)$  for a sensor weighting  $f(x)$  possessing continuous derivatives over its entire length.

Constraints on $f^{(i)}(\pm l/2)$	Rolloff rate in wavenumber $k$		Weighting example
$f(\pm l/2) \neq 0$	$1/k$	-20 dB/decade	Rectangular
$f(\pm l/2) = 0$	$1/k^2$	-40 dB/decade	Triangular
$f(\pm l/2) = 0$ $f'(\pm l/2) = 0$	$1/k^3$	-60 dB/decade	Hanning
$f(\pm l/2) = 0$ $f'(\pm l/2) = 0$ $f''(\pm l/2) = 0$	$1/k^4$	-80 dB/decade	

and its transfer function can be shown to be given by[2]

$$y(k) = \sum_{i=0}^{\infty} \frac{1}{k^{i+1}} \left\{ -f^{(i)}(l/2)e^{-kl/2} + f^{(i)}(-l/2)e^{kl/2} \right\} e^{-kx_0} \quad (2.6)$$

Here we again notice the same general behavior as with the sensor transfer function for spatially sinusoidal strain, namely that the term going as  $1/k$  can be eliminated by setting  $f(\pm l/2) = 0$ . However, due to the fact that the strain is spatially exponential and therefore not oscillatory, there is no further rolloff as with sinusoidal strain.

The transfer functions for rectangular and triangular sensors measuring spatially sinusoidal strain are shown in Figure 2.1. It is clear that the rectangular sensor yields magnitude rolloff of -20 dB/decade in wavenumber, while the triangular sensor yields -40 dB/decade rolloff. For a beam-like structure, temporal frequency  $\omega$  is related,

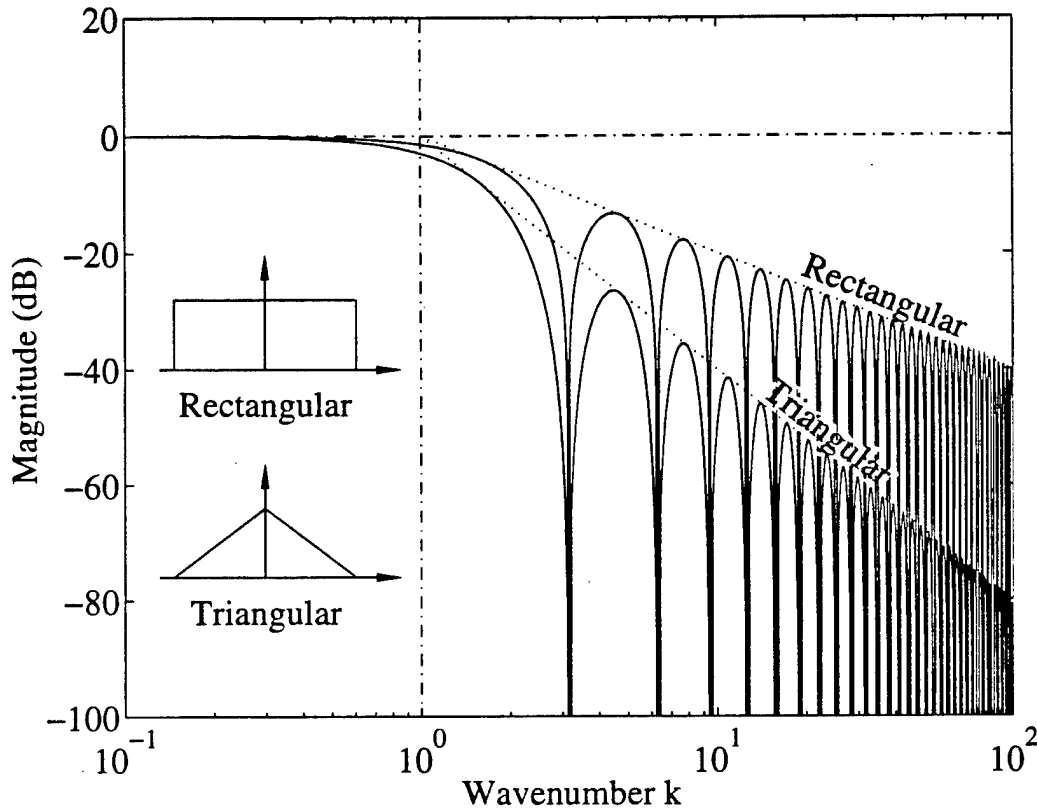







**Figure 2.1:** Transfer functions of rectangular and triangular sensors, including asymptotic behavior at high frequency.

through the dispersion relation, to the square of the wave number ( $k^2$ ). Thus rolloff rates of  $-10$  dB/decade and  $-20$  dB/decade in temporal frequency are possible with rectangular and triangular sensors, respectively.

A number of shapes were considered as candidate spatial weightings for shapes sensors. Such shapes include the Sinc function, Gaussian, rectangular, triangular and Hanning. A summary of their properties is presented in Table 2.2. The sensor lengths are given in terms of the desired rolloff wavenumber,  $k_o$ . The rolloff rates presented are asymptotic. It can be seen in the table that only the shapes with infinite spatial extent have transfer functions which roll off arbitrarily fast. Of the three finite ones, only the triangular sensor has a simple shape and a transfer function

Table 2.2: Properties of shaped sensors with selected weightings.

Sensor Shape	Sensor Length	Rolloff Rate	Negatives in $x$ ?	Finite in $x$ ?	Negatives in $k$ ?
 Sinc	$\infty$	$-\infty$	Yes	No	No
 Gauss	$\infty$	$-\infty$	No	No	No
 Rectangular	$2\sqrt{2}/k_o$	$1/k$	No	Yes	Yes
 Triangular	$4/k_o$	$1/k^2$	No	Yes	No
 Hanning	$\pi\sqrt{2}/k_o$	$1/k^3$	No	Yes	Yes

which contains no negative regions. We therefore consider the triangular sensor to be the best compromise, offering  $1/k^2$  rolloff, with a spatial weighting defined simply by straight line segments.

## CHAPTER 3

---

# Shaped Estimation Schemes

---

An individual sensor provides a single spatially filtered measurement of strain for a certain area of the structure. In order to estimate the shape of the entire structure, an array of such sensors are used. The individual outputs can be numerically integrated to yield slope and displacement estimates. Also, a set of shape functions can be fit to the sensor measurements and then integrated to estimate slope and displacement.

### 3.1 Trapezoidal Integration

The trapezoidal rule is a primitive rule, and in its compound form is given by a Riemann sum of the form

$$T_n(f) = h \left[ \frac{f(a)}{2} + f(a+h) + f(a+2h) + \cdots + f(a+(n-1)h) + \frac{f(b)}{2} \right] \quad (3.1)$$

where  $h = (b-a)/n$  is the number of subdivisions within the interval.

The trapezoidal scheme assumes the function to be integrated, in this case beam curvature, is linear between two successive measurement points. The length of the beam is broken up into intervals between sensor locations, and integrations are per-

formed from the root to successive sensors such that estimates of the slope are available at each sensor location. In this way a second integration step can be performed and displacement estimates can be obtained.

The trapezoidal rule can also be thought of as a way of fitting certain global shape functions to the measurements of the beam curvature. These functions are the linear functions used for first-order finite element analysis, and are 'hat' functions that decrease linearly from the measurement point to zero at the previous and next measurement points, and are zero everywhere else. The curvature is then expressed as a linear combination of these shape functions by multiplying each by a generalized coordinate. Once these coordinates are obtained they are multiplied by the integrals of the shape functions to obtain the slope along the beam. The process can be repeated to obtain displacement estimates.

## 3.2 Simpson's Rule

Simpson's rule is based on approximating the function to be integrated by a quadratic polynomial over three successive sensor locations. These are normally assumed to be equally spaced in order to greatly simplify the resulting expression for the integral. For the case of two subdivisions, this expression is given by

$$\int_a^b f(x) \, dx \approx \frac{(b-a)}{6} \left( f(a) + 4f\left(\frac{a+b}{2}\right) + f(b) \right) \quad (3.2)$$

## 3.3 Modeshape Fitting

The curvature modeshapes of the structure can also be used as a basis and be fitted to the sensor curvature measurement data to approximate the state of the structure.

This has the advantage of using knowledge about the dynamics of the structure in order to make a better estimate and it makes sure that the estimated displacement will automatically satisfy the geometric boundary conditions. We begin by expressing the uncontrolled beam dynamics as

$$\dot{\mathbf{x}} = \mathbf{A} \mathbf{x} + \mathbf{B}_w w \quad (3.3)$$

$$\mathbf{y} = \mathbf{C}_y \mathbf{x} \quad (3.4)$$

$$\mathbf{z} = \mathbf{C}_z \mathbf{x} \quad (3.5)$$

where  $\mathbf{x}$  is a vector of modal displacements and velocities,  $[\mathbf{q} : \dot{\mathbf{q}}]^T$ ,  $\mathbf{y}$  are the available sensor outputs, and  $\mathbf{z}$  is the performance variable we wish to estimate.

Assume the modeshapes of the structure are given by  $\phi_j(x)$  and that the curvature modeshapes are therefore  $\phi_j''(x)$ . The outputs of the sensors is determined by the  $\mathbf{C}_y$  matrix, which for point sensors has entries

$$C_{yij} = \begin{cases} \phi_j''(x_i), & j \leq n \\ 0, & j > n \end{cases} \quad (3.6)$$

and for shaped sensors with spatial weightings  $f_i(x)$  has entries

$$C_{yij} = \begin{cases} \int_0^L f_i(x) \phi_j''(x) dx, & j \leq n \\ 0, & j > n \end{cases} \quad (3.7)$$

where  $n$  is the total number of modes retained in the beam model. We now assume that the performance variable,  $\mathbf{z}$ , is the tip displacement of the beam. It then follows

that the row vector  $C_z$  has the form

$$C_z = \left[ \phi_1(L) \ \phi_2(L) \ \cdots \ \phi_n(L) : 0^{1 \times n} \right] \quad (3.8)$$

Assume there are  $N_y$  sensors and that we wish to use their measurements to fit the first  $N_s$  modes of the structure. We partition the  $C_y$  and  $C_z$  matrices as

$$C_y = \left[ C_{y_1} \ C_{y_2} : 0^{N_y \times n} \right] \quad (3.9)$$

$$C_z = \left[ C_{z_1} \ C_{z_2} : 0^{1 \times n} \right] \quad (3.10)$$

where  $C_{y_1}$  and  $C_{z_1}$  contain the first  $N_s$  columns of  $C_y$  and  $C_z$ , respectively, and where  $C_{y_2}$  and  $C_{z_2}$  are outputs for the  $(n - N_s)$  residual modes. The modal displacements  $p$  of the first  $N_s$  modes can be estimated by assuming that the modal displacements of the residual modes is zero. This is expressed as

$$y = C_{y_1} p \quad (3.11)$$

When the number of assumed modes  $N_s$  and sensors  $N_y$  is equal,  $C_{y_1}$  is square, and if no sensors have been placed at the nodes of any modes,  $p$  can be found by inversion:

$$p = C_{y_1}^{-1} y \quad (3.12)$$

The coordinates  $p$  are then used to find the estimated tip displacement  $\hat{z}$  by computing

$$\hat{z} = C_{z_1} p \quad (3.13)$$

$$= C_{z_1} C_{y_1}^{-1} y \quad (3.14)$$

This scheme will be referred to as the Global Dynamic Shape Function (GDSF) estimation scheme. When the number of assumed modes  $N_s$  is strictly less than the number of sensors  $N_y$ , a least squares approach can be used to compute  $\mathbf{p}$  from (3.11) as

$$\mathbf{p} = \left[ \mathbf{C}_{y_1}^T \mathbf{C}_{y_1} \right]^{-1} \mathbf{C}_{y_1}^T \mathbf{y} \quad (3.15)$$

such that the estimate of the displacement is given by

$$\hat{\mathbf{z}} = \mathbf{C}_{z_1} \left[ \mathbf{C}_{y_1}^T \mathbf{C}_{y_1} \right]^{-1} \mathbf{C}_{y_1}^T \mathbf{y} \quad (3.16)$$

This scheme will be known as the Least Squares Global Dynamic Shape Function (LSGDSF) estimation scheme. This least squares scheme can be modified to include a penalty based on the strain energy present in the first  $N_s$  modes begin fitted to the sensor data [8]. In this case (3.16) is modified:

$$\mathbf{p} = \left[ \mathbf{C}_{y_1}^T \mathbf{C}_{y_1} + \lambda^2 \Lambda_1^2 \right]^{-1} \mathbf{C}_{y_1}^T \mathbf{y} \quad (3.17)$$

where  $\Lambda_1 = \text{diag} \{ \omega_1 \ \omega_2 \ \cdots \ \omega_{N_s} \}$ . The estimated tip displacement is then given by

$$\hat{\mathbf{z}} = \mathbf{C}_{z_1} \left[ \mathbf{C}_{y_1}^T \mathbf{C}_{y_1} + \lambda^2 \Lambda_1^2 \right]^{-1} \mathbf{C}_{y_1}^T \mathbf{y} \quad (3.18)$$

It can be seen that this reduces to the LSGDSF scheme for zero strain energy weighting  $\lambda^2$ . It was seen in simulations that the effect of the spatial aliasing of the higher modes could be reduced by penalizing them heavily. However, this has the effect of introducing magnitude errors in the estimation of the lower modes.



### 3.4 Kalman Filter

A Kalman Filter can also be used to generate estimates of all the modeled modal states using the  $N_y$  sensors. Assume that the filter incorporates the first  $N_s$  modes of the structure:

$$\dot{\hat{\mathbf{x}}} = \mathbf{A}_1 \hat{\mathbf{x}} + \mathbf{B}_w w + \mathbf{H} [\mathbf{y} - \hat{\mathbf{y}}] \quad (3.19)$$

$$\hat{\mathbf{y}} = [\mathbf{C}_{y_1} : \mathbf{0}^{N_s \times N_s}] \hat{\mathbf{x}} + v \quad (3.20)$$

$$\hat{\mathbf{z}} = [\mathbf{C}_{z_1} : \mathbf{0}^{1 \times N_s}] \hat{\mathbf{x}} \quad (3.21)$$

where  $\mathbf{A}_1$  incorporates the dynamics of the first  $N_s$  modes only, such that  $\mathbf{A}_1 = \begin{bmatrix} \mathbf{0} & \mathbf{I} \\ -\Lambda_1^2 & \mathbf{0} \end{bmatrix}$ , and  $w$  and  $v$  are process and sensor noises, respectively.

It is now shown how a static form of the Kalman filter has a very similar form to the weighted LSGDSF scheme. If the filter dynamics are neglected, we set  $\dot{\hat{\mathbf{x}}} = 0$  to obtain

$$\hat{\mathbf{x}} = [\mathbf{C}_{z_1} : \mathbf{0}] [-\mathbf{A}_1 + \mathbf{H} [\mathbf{C}_{y_1} : \mathbf{0}]]^{-1} \mathbf{H} \mathbf{y} \quad (3.22)$$

If the Kalman filter gain matrix  $\mathbf{H}$  is partitioned into  $\mathbf{H} = \begin{bmatrix} \mathbf{H}_1 \\ \mathbf{H}_2 \end{bmatrix}$ , we obtain

$$\hat{\mathbf{z}} = [\mathbf{C}_{z_1} : \mathbf{0}] \begin{bmatrix} \mathbf{H}_1 \mathbf{C}_{y_1} & -\mathbf{I} \\ \mathbf{H}_2 \mathbf{C}_{y_1} - \Lambda_1^2 & \mathbf{0} \end{bmatrix}^{-1} \mathbf{H} \mathbf{y} \quad (3.23)$$

which can be simplified to yield

$$\hat{\mathbf{z}} = \mathbf{C}_{z_1} [\mathbf{H}_2 \mathbf{C}_{y_1} + \Lambda_1^2]^{-1} \mathbf{H}_2 \mathbf{y} \quad (3.24)$$

This result is of the same form as (3.18) with  $C_{v1}^T$  replaced by  $H_2^T$  and  $\lambda^2 = 1$ . Interestingly,  $H_2$ , the bottom half of the Kalman filter gain matrix corresponds to the weightings applied to the differences between estimated and actual outputs before feedback to the velocity states of the filter. Retaining all the dynamics of the filter yields the estimate

$$\hat{z} = [C_{z1} \ : \ 0] [sI - A_1 + H [C_{v1} \ : \ 0]]^{-1} H y \quad (3.25)$$

As the assumed noise level on the sensors is reduced,  $H_1$  approaches zero, and the above expression can be simplified to yield

$$\hat{z} = C_{z1} [H_2 C_{v1} + (\Lambda_1^2 - s^2 I)]^{-1} H_2 y \quad (3.26)$$

which simplifies to the static Kalman filter which  $s = 0$  and which is seen to roll off at very high frequency.

## 3.5 Boundary Problems

Many integration schemes require knowledge of the measurand to be integrated at the boundaries of the interval. These boundary measurements can be made using a sensor centered at the boundary. However, it has been shown in [2] that care must be exercised in the implementation of such sensors. The truncation required limits the high frequency rolloff to at most  $1/k$ , or  $-10$  dB/decade in temporal frequency for a beam-like structure. This can be problematic at high frequency where limited observability to the higher order dynamics of the structure is desirable.

A second option exists in which the curvature at the boundary of the structure is inferred by using a combination of the measurements of the sensors closest to that

boundary. For example, this could take the form of a linear extrapolation using two sensor measurements or a quadratic extrapolation using three sensors. It is generally seen that at high frequency, extrapolation schemes yield unacceptable estimates for the root curvature, and the limited rolloff of a sensor truncated at the boundary yields better results.

## CHAPTER 4

---

# Shape Estimation of Pinned-Pinned Beam

---

### 4.1 Description

In this section we investigate the performance of an array of point or spatially averaging strain sensors for the purposes of estimating the dynamic mode shapes of a pinned-pinned beam. It is assumed that the performance variable to be estimated is the tip slope of the and this is computed using various estimation schemes. This is accomplished by simulating a Bernoulli-Euler model of the beam fitted with point and shaped sensors. The beam is actuated by a point moment at the tip, and the collocated tip moment to tip slope response is estimated using the sensor arrays.

In the simulations it was assumed that there were 7 sensors equally spaced in the interior of the beam, such that the  $i$ -th sensor is centered around the point  $iL/8$  where  $L$  is the length of the beam. It is further assumed that any sensor which falls partially beyond the boundary of the beam is simply truncated. The lost area of the sensor is accounted for by requiring that the sensor gain be unity in order to correctly measure constant strain signals.

A variety of simple integration rules, including the trapezoidal and Simpson's

**Table 4.1:** Estimation errors of various integration schemes in estimating the response of the tip slope of a pinned-pinned beam.

	Point Sensors	Triangular Sensors
Trapezoidal	3.359	3.553
Simpson	2.790	2.298
GDSF	7.184	7.379
LSGDSF-4	6.903	7.697

rules, as well as the GDSF and LSGDSF fitting schemes were used to integrate curvature measurements made by the sensors in order to estimate the tip slope.

It is assumed that the curvature is zero at the root and tip of the beam. The initial slope at the root of the beam that is required by the trapezoidal and Simpson's rules is computed by first assuming it is zero, then estimating the resultant beam tip displacement. The tip displacement is then set to zero by effectively rotating the estimated orientation of the beam by changing the slope at the root.

In Table 4.1 are summarized some estimation error measures for various integration schemes. In these schemes seven equally spaced point or triangular sensors were used. The triangular sensors were all one quarter of the beam length. The estimation error measure has been used previously in the identification of structures [7] and penalizes the log of the ratio of the actual and estimated response:

$$J = \frac{1}{N} \sum_{i=1}^N \left| \log \left( \frac{\hat{G}(f_i)}{G(f_i)} \right) \right|^2 \quad (4.1)$$

where  $G(f_i)$  is the actual response and  $\hat{G}(f_i)$  is the estimated response of the beam. The frequency range over which the performance measure was computed was between 10 Hz and just beyond the 14<sup>th</sup> mode. This range was chosen based on this mode being twice the number of sensors in the array. Modes beyond the number of sensors

are difficult to estimate accurately, and modes 8–14 lie in the first range of modes that contribute to spatial aliasing in the sensor array measurements.

The table shows that the schemes which seem to perform best are the trapezoidal and Simpson's rules, rather than the modeshape fitting schemes. The GDSF scheme fits seven modeshapes to the seven sensor measurements, while the LSGDSF-4 scheme fits, in a least squares sense, the first four modeshapes to the seven sensor measurements.

It is also seen in the table that the triangular sensors do not seem to offer significant advantages over point sensors. The error measure does not distinguish between the magnitude of the estimated response being larger or smaller than the theoretical response. However, when using the triangular sensors, significant rolloff in the sensor outputs is introduced. This has the effect of making the estimated response roll off at high frequency. When using point sensors, the magnitude of the estimated response actually increases for the higher modes, thus yielding more observation spillover.

It should also be noted that there were significant estimation errors at low frequency, but to the fact that the static mode cannot be represented accurately using a combination of the dynamic mode shapes. This error contributes significantly to the estimation error measure at low frequency.

## 4.2 Trapezoidal Rule

Figure 4.1 shows the estimated tip slope response to a tip moment disturbance by using arrays of point and triangular sensors in conjunction with the trapezoidal rule. We see generally acceptable estimation performance up to about the fifth mode. Beyond this point, the trapezoidal rule is unable to accurately follow the curvature

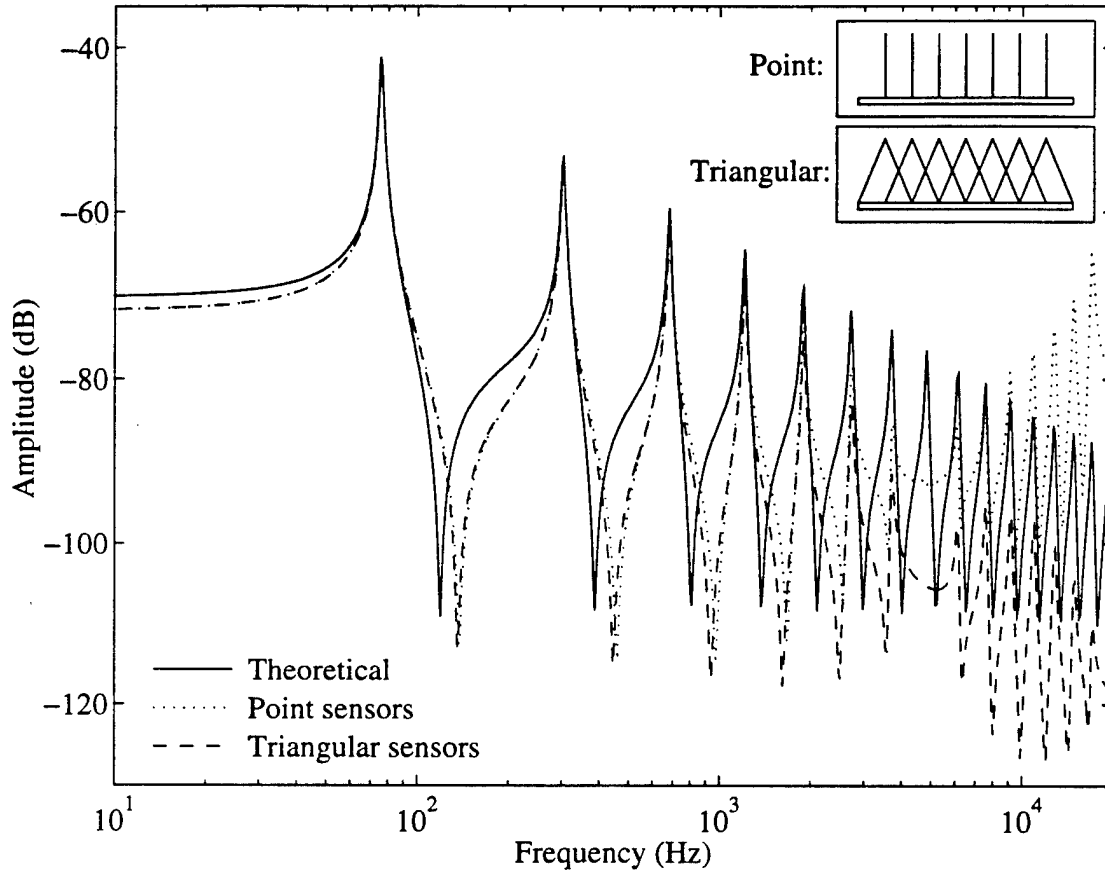


**Figure 4.1:** Estimate of the tip slope response given a tip moment disturbance, using point and triangular sensors with the trapezoidal rule.

profiles of modes with higher spatial frequency. The estimates decrease in magnitude until about the eighth mode, at which point the magnitude of the estimated response increases rapidly due to spatial aliasing and quickly rises beyond the theoretical response. Using the triangular sensors, we see good estimation performance for the first five modes. Beyond this point, we see a decrease in the estimated modal amplitudes, even including spatial aliasing. It can be seen from the unstable high frequency behavior found with the point sensors that the added rolloff the triangular sensors offer is very important in keeping the estimated response bounded at high frequency. For both schemes, a static estimation error is present, and this contributes

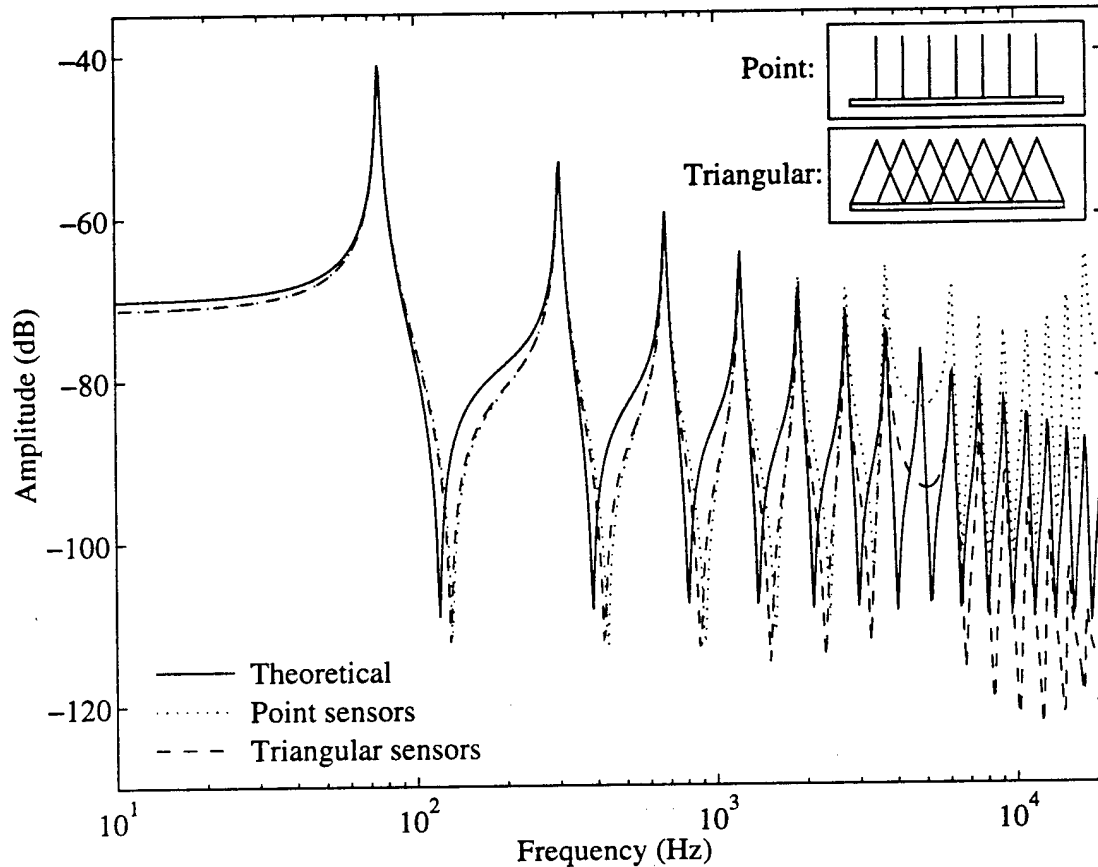


Figure 4.2: Estimate of the tip slope response given a tip moment disturbance, using point and triangular sensors with the trapezoidal rule.

to the problems seen in accurately estimating the frequency of the low order zeros.

## 4.3 Simpson's Rule

The estimated tip slope response to a tip moment input is shown in Figure 4.2 when using Simpson's rule as the estimation scheme. For this scheme we find slightly better performance up to about the sixth mode when using the point sensors. When using the estimates obtained with triangular sensors, better estimates of the amplitude of the seventh mode are obtained. The eighth mode is once more unobservable, and beyond this point we see the estimates using the point sensors generally increasing in



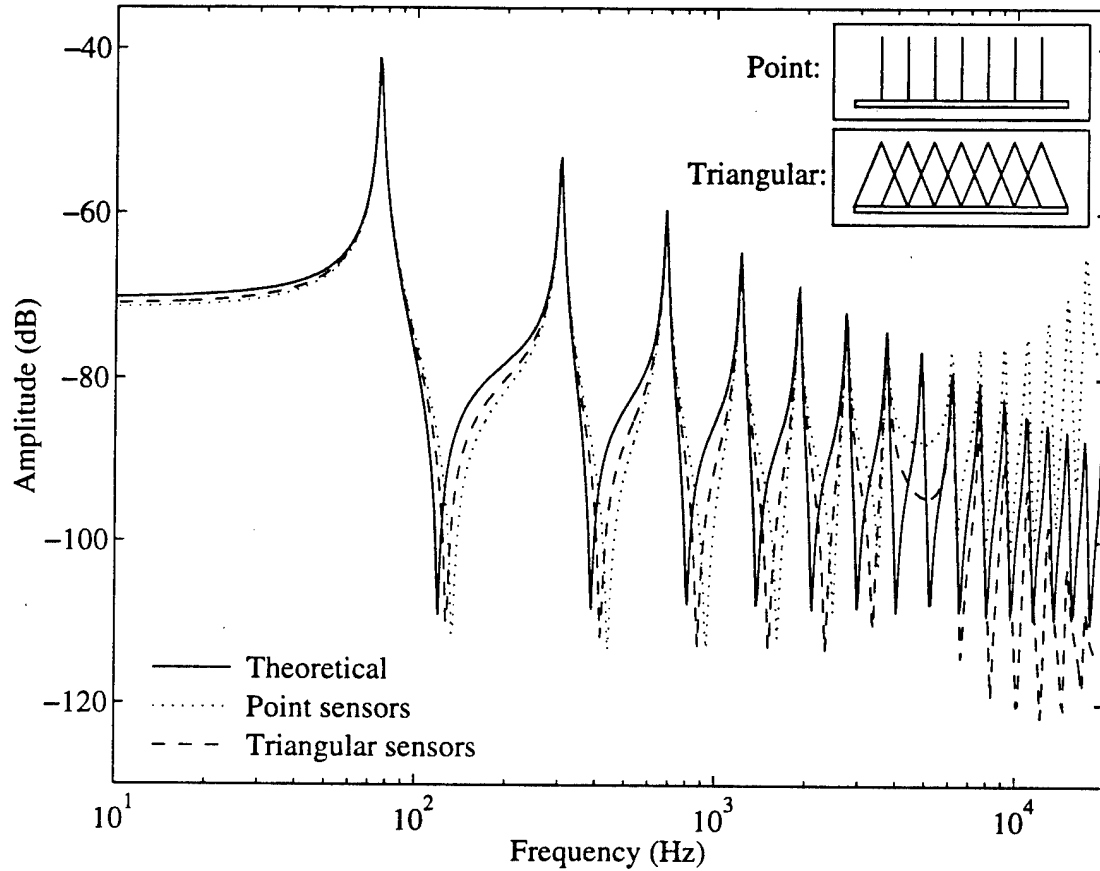


Figure 4.3: Estimate of the tip slope response given a tip moment disturbance, using point and triangular sensors with the GDSF scheme.

amplitude, while those obtained using the triangular sensors tend to roll off at these higher frequencies.

## 4.4 GDSF Scheme

Figure 4.3 shows the estimated response for the pinned-pinned beam using point and triangular sensors with the global dynamic shape function fitting scheme (GDSF). This scheme fits the modeshapes of the beam to the sensor measurements, and this already guarantees that the geometric boundary conditions will be satisfied by the estimated solution. It can be seen that using point sensors yields good estimates

for the first seven modes, since a sum of the first seven modeshapes are being fit to the sensor data. Beyond this, spatial aliasing becomes a problem and the estimated response grows much larger in magnitude than theory predicts. Using triangular sensors solves this problem by introducing rolloff of the sensors to the higher modes. The first seven modes are accurately observed using the triangular sensors, and the results are very similar to those obtained using points sensors. However, beyond this frequency, errors due to spatial aliasing are highly reduced as compared to point sensors by virtue of the rolloff of the triangular sensors.

## 4.5 LSGDSF Scheme

The estimated and theoretical tip slope response when using the least squares global dynamic shape function fitting scheme with four shape functions and with rectangular and triangular sensors is shown in Figure 4.4. In this scheme four shapes are fit to the seven sensor measurements in a least squares sense, and also guarantees that the geometric boundary conditions will be satisfied. We find excellent performance in terms of estimating the amplitude of the first four modes, using both rectangular and triangular sensors. Unfortunately, the frequencies of the first three zeros is slightly worse using this scheme than for the GDSF scheme, due to the smaller number of shape functions fit to the sensor measurements. Beyond the fourth mode there is very little response to any mode up until mode 12. At this point the response estimated using triangular sensors is much larger than when using triangular sensor measurements, and the trend closely resembles the GDSF scheme results.

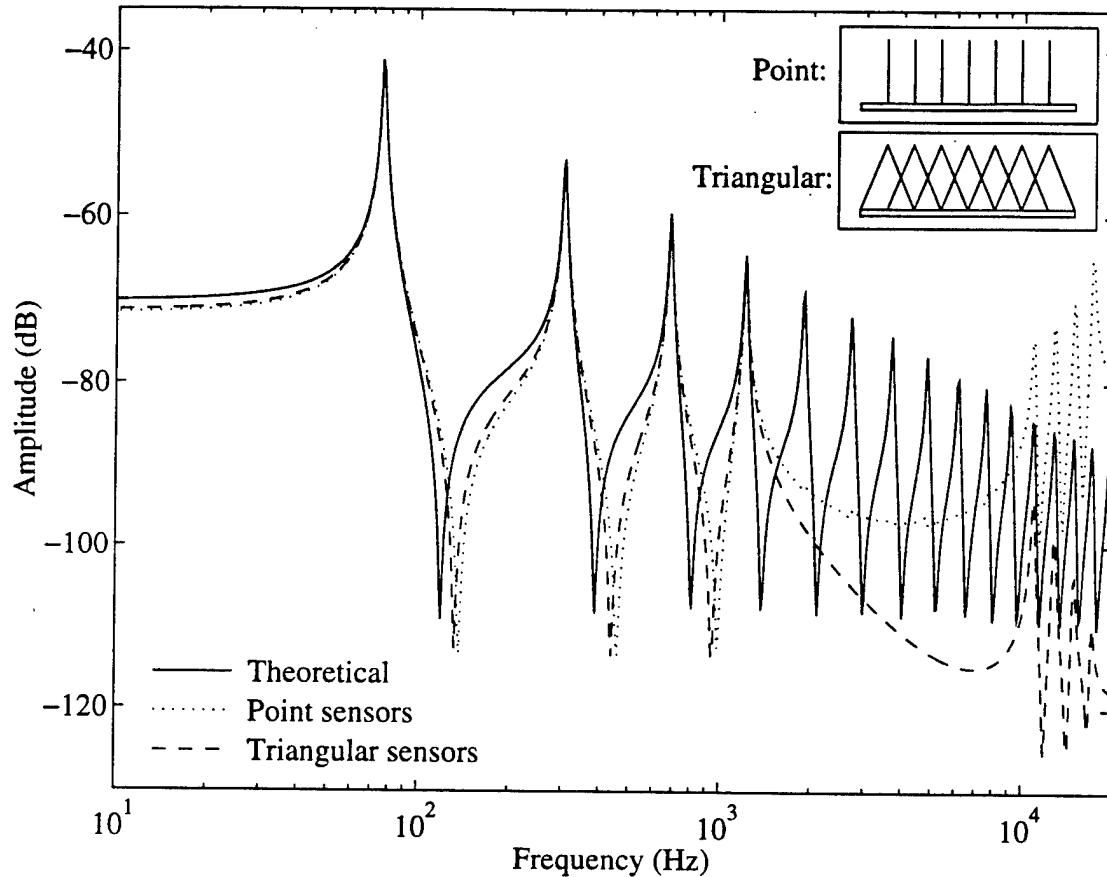


Figure 4.4: Estimate of the tip slope response given a tip moment disturbance, using point and triangular sensors with the LSGDSF scheme when fitting four shape functions.

## 4.6 Summary

In general it was found that the GDSF scheme yielded the best results for low order modes. While the trapezoidal and Simpson schemes were only able to follow the oscillations of the first five or six modes, the GDSF scheme was able to generate good estimates up to the seventh mode, while the LSGDSF scheme generated good estimates up to the mode corresponding to the number of global shape functions (modeshapes) which were retained and fit to the sensor data.

---

Beyond the seventh mode, where spatial aliasing is a severe problem, it is clear that it becomes critical to use the measurements shaped sensors. This is because their output rolls off at high frequency, making higher modes which are outside the control bandwidth less observable and thus prevent them from producing undesirable effects in the estimated response.

## CHAPTER 5

---

# Shape Estimation of Clamped-Free Beam

---

### 5.1 Description

Now the performance of an array of shaped sensors used to estimate the dynamic mode shapes of a clamped-free beam is investigated. It is again assumed that there are 7 equally spaced sensors in the interior, but an additional sensor centered at the root was employed in all cases in an attempt to perform more accurate root curvature estimation. The performance variable was assumed to be the displacement of the tip and a tip force disturbance was used to disturb the beam.

The exponential components of the clamped-free mode shapes at the root and tip makes tip deflection estimation a much harder problem than tip slope estimation for a pinned-pinned beam with purely spatially sinusoidal mode shapes. Specifically, good knowledge of the strain at the root is required for good estimation of the tip deflection for low order modes. However, for higher order modes, measurements of the root strain should roll off as quickly as measurements of strain in the interior of the beam.

A variety of integration schemes were again used to integrate the measurements

**Table 5.1:** Estimation errors of various integration schemes in estimating the response of the tip displacement of a clamped-free beam.

No root sensor		
Scheme	Point Sensors	Triangular Sensors
Trapezoidal	9.979	5.517
Simpson	10.201	5.595
GDSF	12.834	7.800
LSGDSF-4	9.642	5.355
Including root sensor		
Scheme	Point Sensors	Triangular Sensors
Trapezoidal	7.484	0.901
Simpson	6.892	3.403
GDSF	5.245	0.671
LSGDSF-4	9.806	2.309

made by the sensor array and estimate beam tip displacement. For the trapezoidal and Simpson integration schemes, the sensor measurements were assigned at the centers of the interior sensors and at the root for the cases where there was a half-sensor centered there. The sensor measurements were again simulated using a Bernoulli-Euler model of a clamped-free beam and the various estimation schemes were used to estimate the tip displacement.

Table 5.1 shows the estimation error measure when trying to estimate the tip displacement of a clamped-free beam. These error measures were computed in the same way as for the pinned-pinned beam and show that significantly improved performance is possible when using a sensor placed at the root of the beam. This is

because the estimated tip displacement is highly sensitive to the root curvature. It is therefore concluded that a sensor placed at the boundary of the structure is critical to good shape estimation performance.

What is also clear from the results is that the GDSF scheme performs significantly better than the LSGDSF scheme. Therefore it does not make sense to use the a shape fitting schemes with fewer mode shapes than sensors. The results also indicate that improvements in the error are afforded by using triangular sensors, indicating yet again that the rolloff of shaped sensors can be used effectively in structural shape estimation.

## 5.2 Trapezoidal Rule

The estimation performance of the trapezoidal rule when using an array of seven internal point or triangular sensors is shown in Figure 5.1. We see good performance in estimating the amplitudes of the first three modes, and the frequencies of the first two zeros. Beyond this point the third mode is badly estimated and most of the subsequent zeros are missed altogether. Between the fourth and ninth modes the results using point and triangular sensors differ little, although the error obtained with the triangular sensors are decreasing as the outputs roll off. Beyond the eighth mode there is significant spatial aliasing and the errors obtained with triangular sensors are much lower than those found when using point sensors. It is at these frequencies that the rolloff of the triangular sensors becomes highly beneficial.

A sensor was then centered at the root in order to estimate root curvature more accurately, and seven more sensors were equally spaced in the interior of the beam. Figure 5.2 shows the estimated tip displacement response to a tip force disturbance when using the additional root-centered point and triangular sensors with the trape-

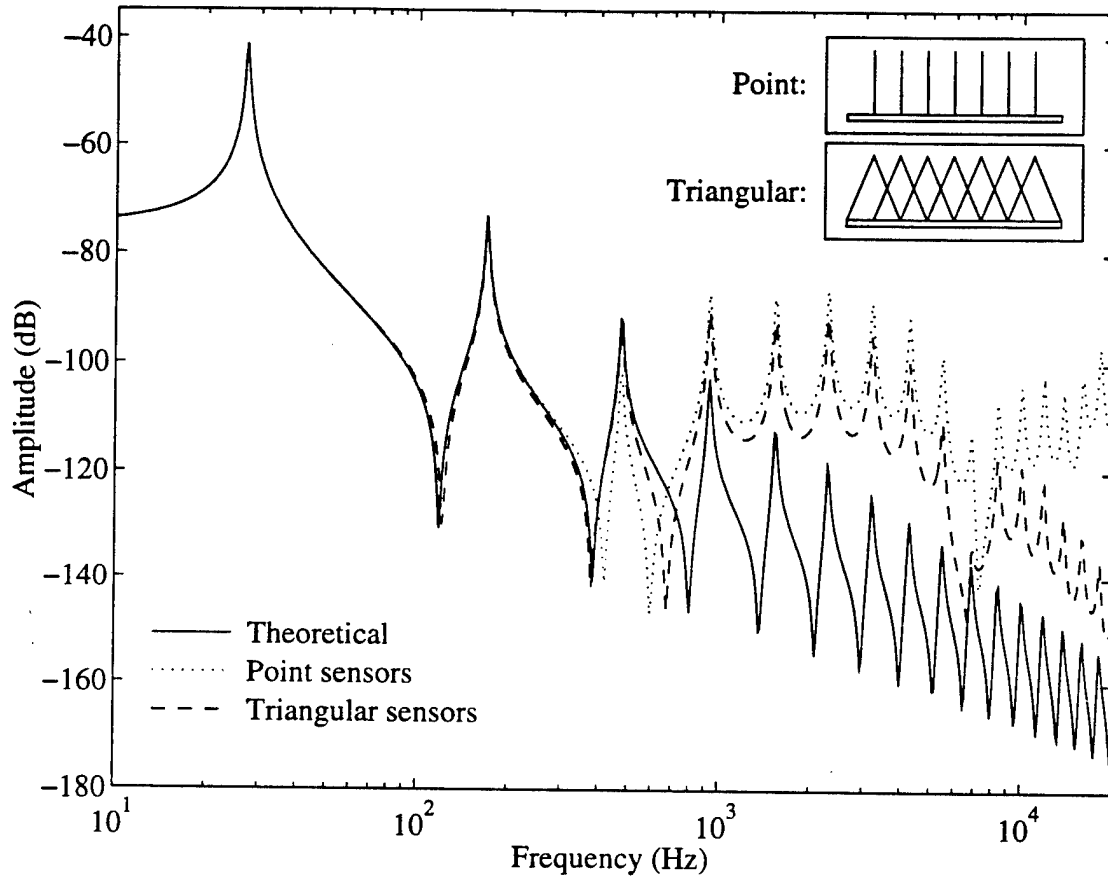


**Figure 5.1:** Estimate of the tip deflection response given a tip force disturbance, using an array of seven point and Triangular sensors with the trapezoidal rule.

zoidal rule. It can be seen that when using point sensors, good estimates are available to about the fourth mode, with only the first two zeros being well-resolved. Beyond the fourth mode, however, the estimated magnitude of the response begins to increase well beyond those of the theoretical response. Using an array of triangular sensors improves performance considerably and yields a good estimate of the response for all low order modes. The errors due to spatial aliasing have very little impact on the estimated response, thanks to the root curvature measurement and the rolloff provided by the triangular sensors.



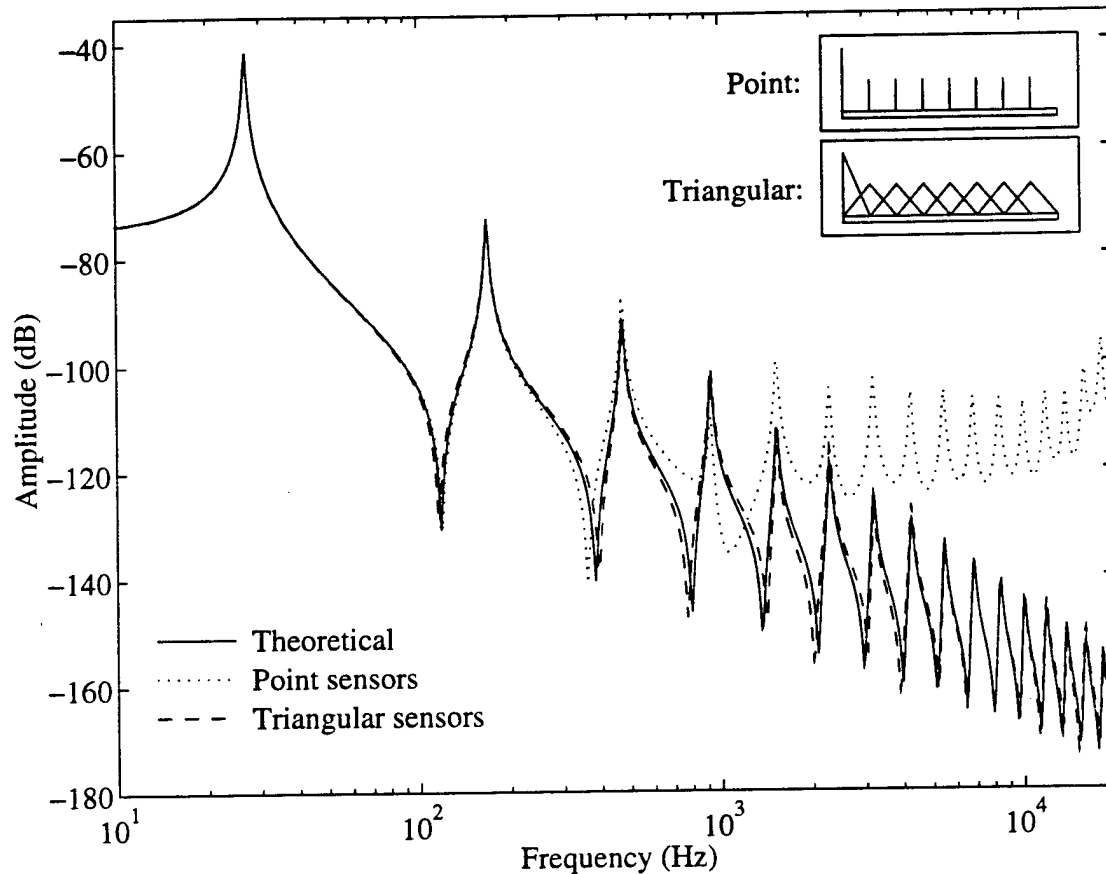


**Figure 5.2:** Estimate of the tip deflection response given a tip force disturbance, using an array of eight point and Triangular sensors with the trapezoidal rule.

## 5.3 Simpson's Rule

Figure 5.3 shows the estimation performance obtained when using seven internal point and triangular sensors in conjunction with Simpson's rule. The performance obtained is very similar to the results using the trapezoidal rule. The first three modes are reasonably well predicted, but only the first zero is resolved with the point sensors, while the first two zeros are resolved reasonably well with the triangular sensors. The performance using both point and triangular sensors is very similar between modes four and ten, although the observability of the modes to the triangular sensors is

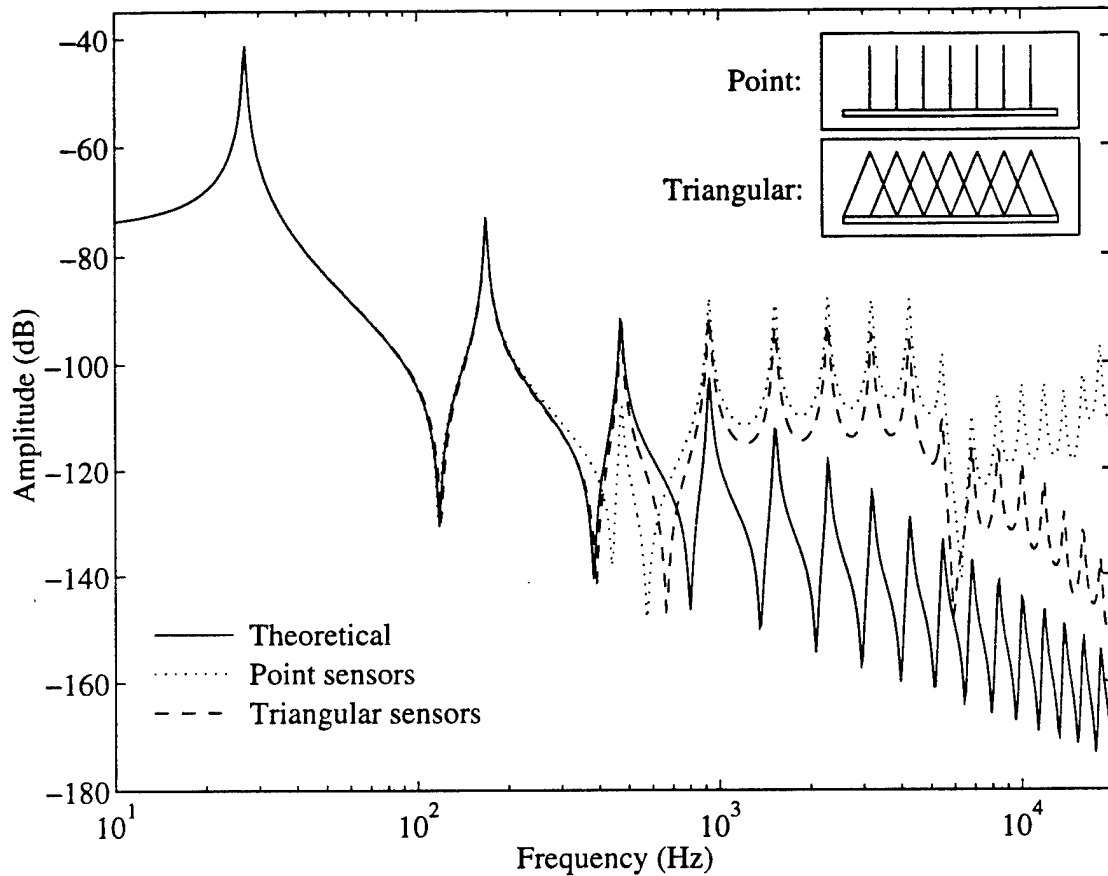


**Figure 5.3:** Estimate of the tip deflection response given a tip force disturbance, using point and Triangular sensors with Simpson's rule.

clearly beginning to decrease with respect to the point sensors. Beyond the tenth mode there is significant rolloff of the triangular sensor estimates as compared with the point sensors, demonstrating the pronounced rolloff of the shaped sensor at higher frequency.

The effects of adding a measurement from a root-centered sensor are shown in Figure 5.4. It can be seen that as with the trapezoidal rule, significant performance improvements are evident for both sensor types. When using point sensors, the first five modes and first three zeros are predicted very accurately, but there is a slight error in the frequency predicted for the fourth zero. The predictions obtained with the

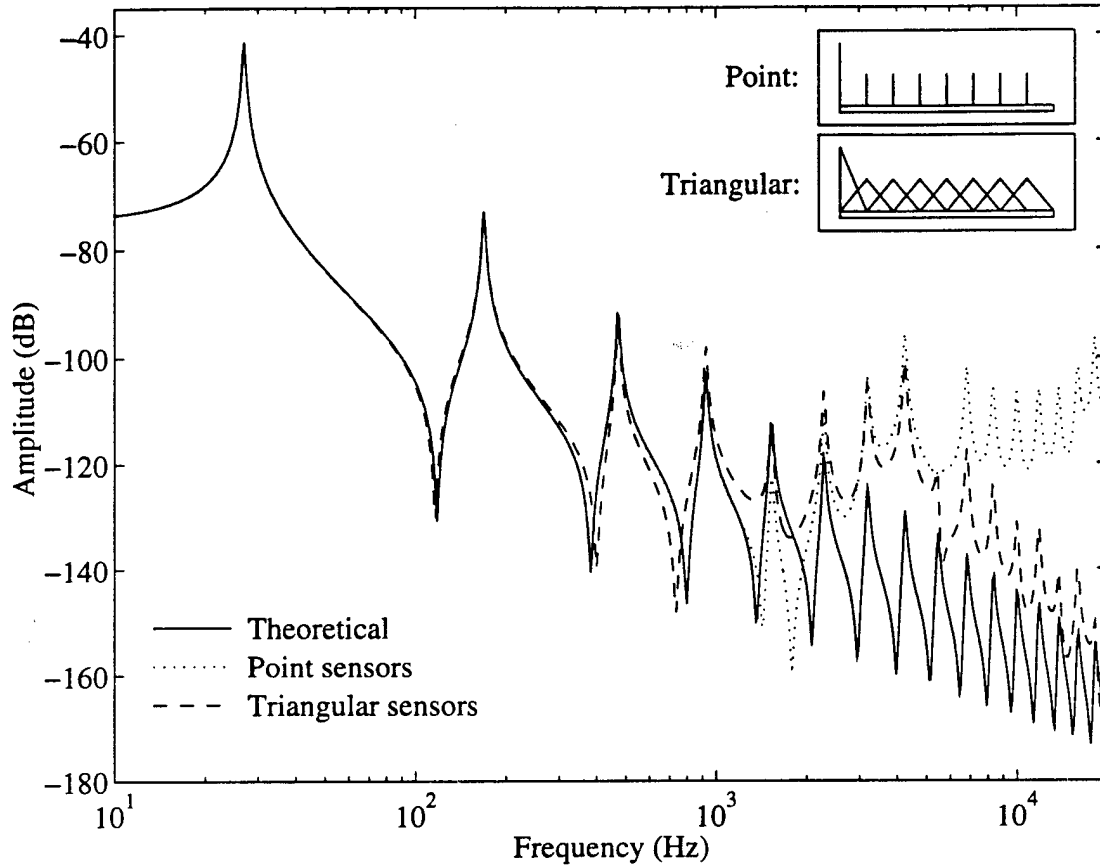


**Figure 5.4:** Estimate of the tip deflection response given a tip force disturbance, using point and Triangular sensors with the Simpson's rule.

triangular sensors are actually a little worse, as only the first three zeros are present in any significant way. However, the amplitude of mode five is more accurately observed using triangular sensors than with point sensors. Beyond mode five both sensors have problems with spatial aliasing, but sensor rolloff affects the triangular sensor outputs significantly beyond mode 8, greatly reducing estimation errors at high frequency.

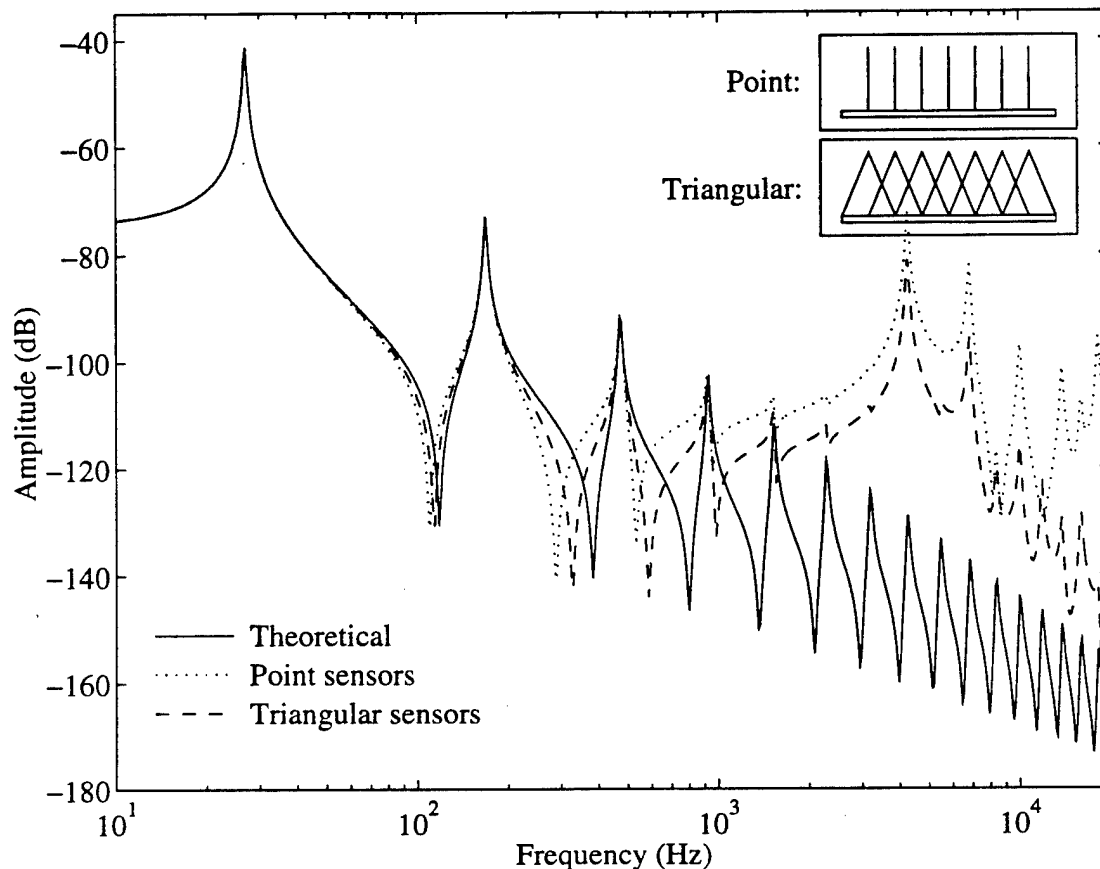


**Figure 5.5:** Estimate of the tip deflection response given a tip force disturbance, using point and triangular sensors with the GDSF rule.

## 5.4 GDSF Scheme

The sensors arrays used in conjunction with the trapezoidal rule discussed above were also used with the GDSF scheme. The results when using seven internal sensors and no root sensor are shown in Figure 5.5. Both sensors offer good performance for only the first two modes. Beyond this point significant observation spillover from the poor estimation of the eighth mode corrupts the estimates of the frequencies of the low order zeros. Larger and larger errors are obtained using both sensor types as mode eight is approached. At mode eight, severe spatial aliasing problems result as the GDSF scheme attempts to fit a combination of the first seven modes to the aliased

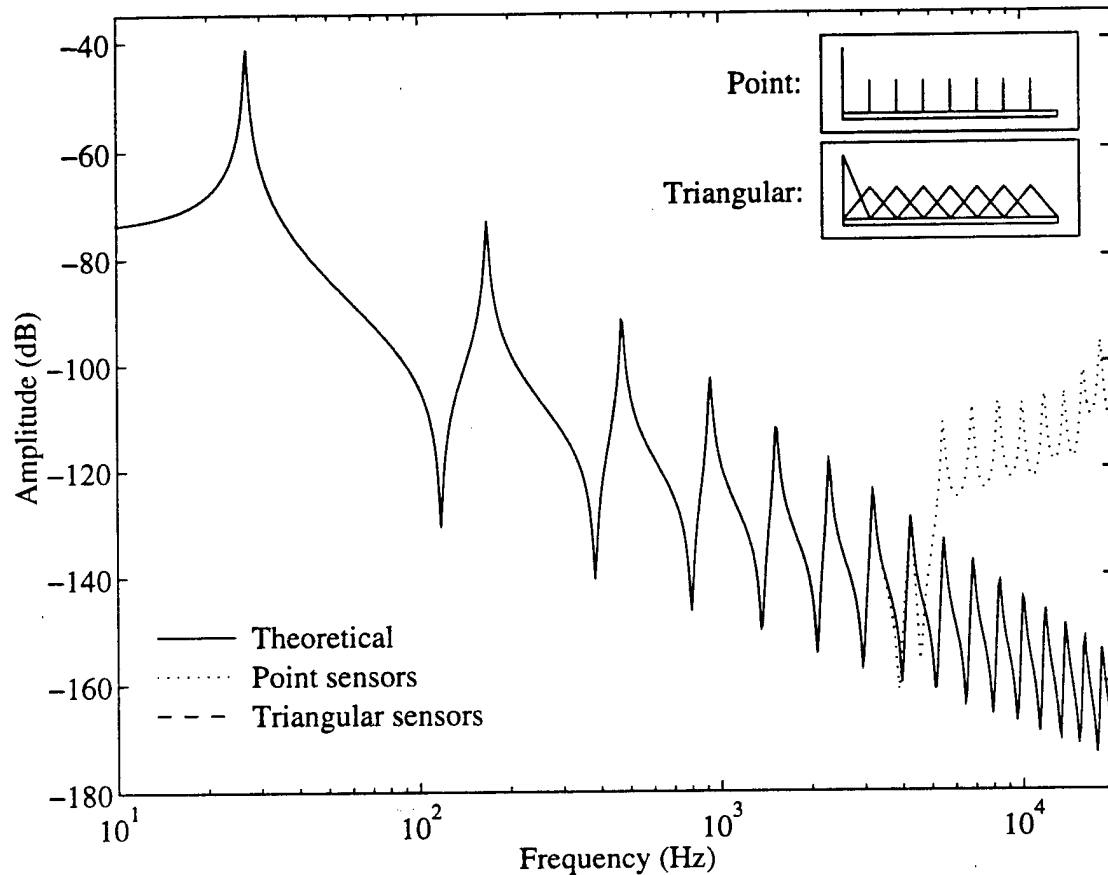


**Figure 5.6:** Estimate of the tip deflection response given a tip force disturbance, using point and triangular sensors with the GDSF rule.

measurements of the eighth mode. Although errors are large for both sensor types beyond the eighth mode, these errors are significantly lower for the triangular sensors, especially as the frequency is increased.

The results when using the GDSF scheme with an additional root sensor shown in Figure 5.6. Using point sensors, very good estimation performance is now seen for the first eight modes, since now the first eight mode shapes are being fit to the sensor outputs. Beyond the eighth mode, severe spatial aliasing problems are observed. This results in a general increase in the magnitude of the estimated response and a deterioration in estimation performance. Again, this situation is remedied by using

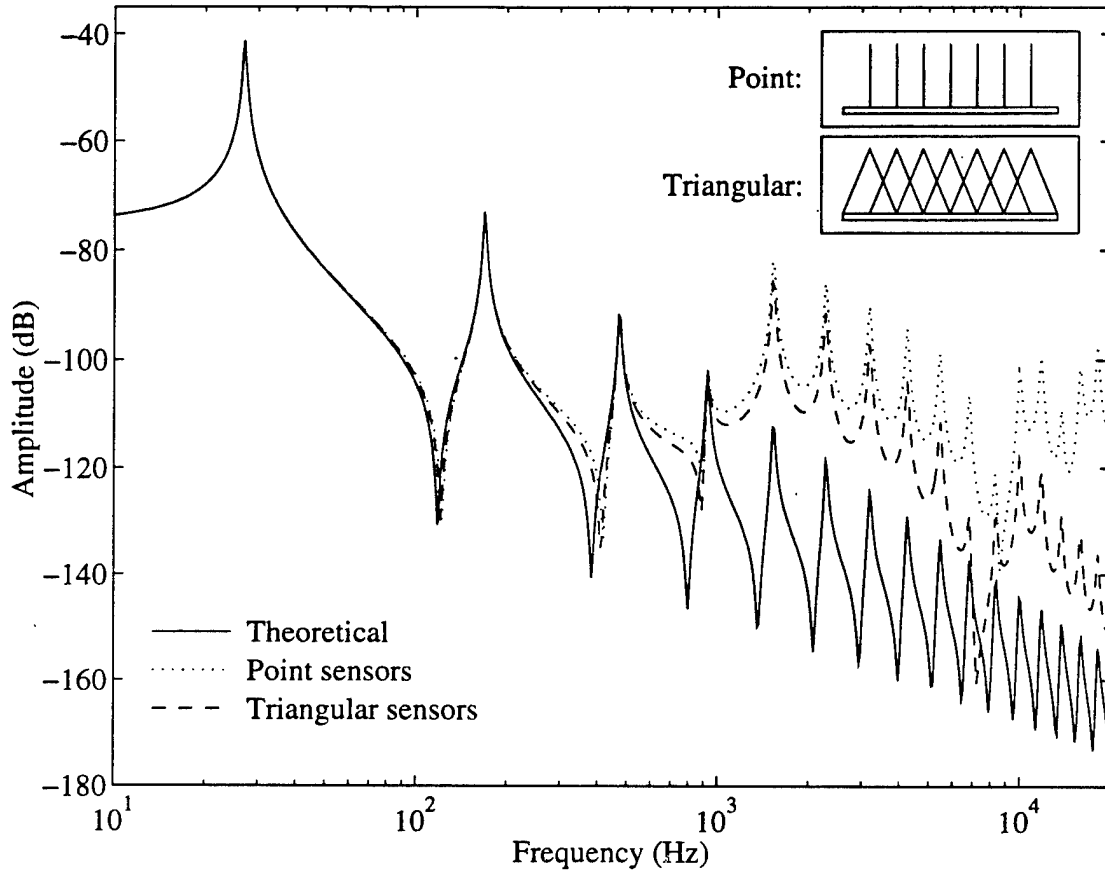


**Figure 5.7:** Estimate of the tip deflection response given a tip force disturbance, using point and triangular sensors with the LSGDSF rule.

triangular sensors. Such sensors offer rolloff to higher order modes, and this is seen in the behavior of the estimated response beyond the eighth mode. In this region the estimated response remains bounded and its rolloff is secured. This stable behavior is not possible without the presence of the half-sensors centered at the root of the beam. This sensor is critical in estimating the root curvature, to which the estimated tip displacement is very sensitive.

## 5.5 LSGDSF Scheme

Figure 5.7 shows the tip displacement estimation performance obtained using arrays

of seven internal point and triangular sensors in conjunction with the least squares global dynamic shape function fitting scheme for the case where the shapes of the the first four modes are used. For both sensor types we see good performance for the first two modes, and then deteriorating performance, especially in the identification of the zeros, up to mode four. Beyond this point spatial aliasing prevents the scheme from keeping up with the higher spatial frequencies of mode five and beyond, and severe estimation error are observed. Up through mode nine or ten we see the same general trend of missing zeros for both the point and triangular sensors, with the characteristic rolloff associated with the triangular sensors. Beyond mode ten the estimates using point and triangular sensors diverge as the triangular sensor outputs roll off substantially as compared to the point sensor estimates, which actually increase with frequency.

Figure 5.8 shows the estimation performance when fitting four mode shapes to the outputs of eight point or triangular sensors, including a sensor centered at the beam root. It is seen that there is definite improvement in performance as compared to the previous sensor layout omitting a root-centered sensor. The first four poles and three zeros are accurately observed using both point and triangular sensors. There are significant errors in the frequency of the fourth mode, and beyond this point significant errors related to spatial aliasing occur, as expected. Also, as expected, the rolloff of the triangular sensors greatly decreases the estimation errors as compared to the point sensors, especially beyond mode nine.

## 5.6 Summary

It has been shown how estimation schemes using triangular sensors generally perform better than the same scheme employing point sensors. It is consistently seen that at

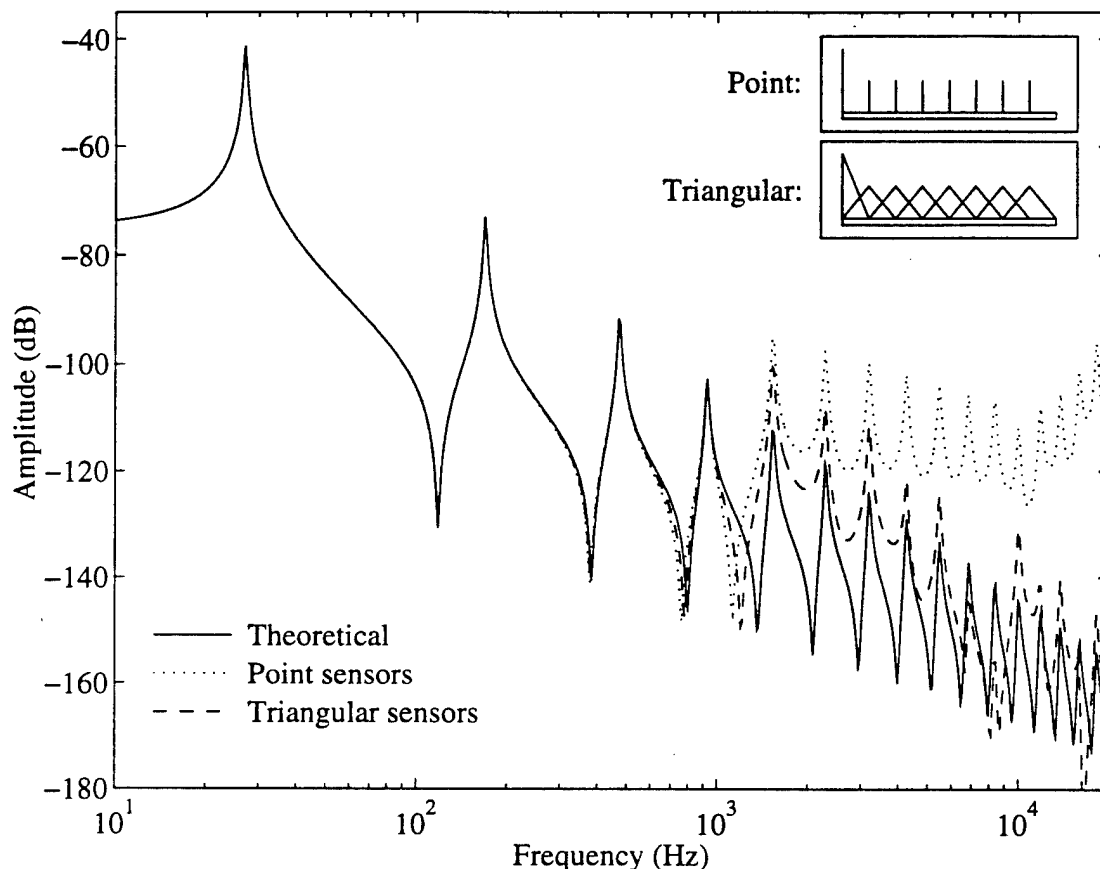


**Figure 5.8:** Estimate of the tip deflection response given a tip force disturbance, using point and triangular sensors with the LSGDSF rule.

higher frequency, when spatial aliasing has a significant impact on performance, that the reduced observability of the triangular sensors is critical in bounding the error. This reduction in error is particularly pronounced beyond mode ten.

It has also been shown that the estimation performance is very similar when using the trapezoidal or Simpson's rules. In one particular case, using eight triangular sensors, the trapezoidal rule offers better results than Simpson's rule. When comparing the GDSF and LSGDSF schemes, it is clear that when a root sensor is available, it makes sense to use the GDSF scheme to accurately fit as many modes as possible to the sensor measurements. If, however, no root sensor is available, then



---

the severe observation spillover resulting from spatial aliasing of a high mode is best mitigated by using fewer shapes than sensors.

## CHAPTER 6

---

# Experimental Shape Estimation Results

---

In order to determine the ability of a shaped sensor array to estimate the deflection of a beam-like structure, an effort was made to experimentally implement some of the cases studied in the simulations for the case of a cantilevered beam.

### 6.1 Description

An aluminium beam 30 inches long was manufactured and was mounted in a cantilever configuration. The beam had a T-shaped cross-section, with a top flange 2 inches wide, and a central flange 1 inch deep. The top and central flanges were both  $1/4$  inch thick. The beam had a first bending frequency of about 28 Hz.

On the top flange, 22 Bartlett (triangular) sensors were fabricated by etching the electrode of PVDF piezoelectric film. The film used was 28-microns thick with sputtered nickel-copper electrodes and was manufactured by Kynar/Pennwalt Corporation. The shapes of the sensors were drawn directly on one side of the film electrode using a permanent pen, leaving thin lines of electrode visible between adjacent sensors. The remaining electrode not masked by the permanent ink was etched using a heavily diluted ferric chloride solution. The length of each sensor was  $1/8$  of the beam

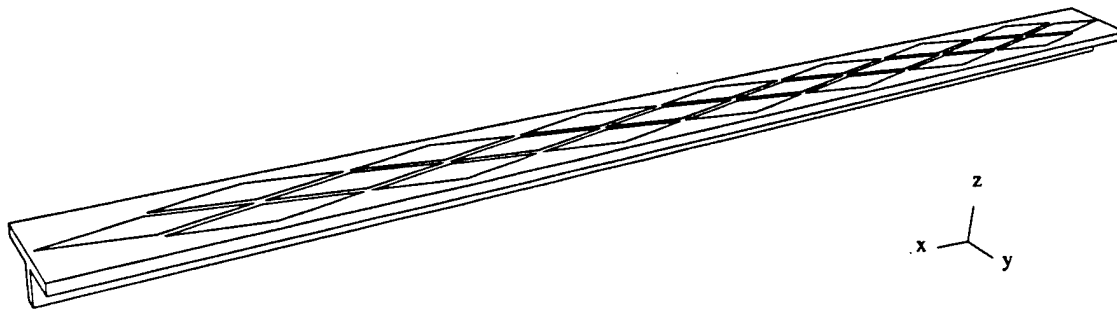


**Figure 6.1:** Perspective view of T-Section beam with arrangement of array of 22 Bartlett sensors.

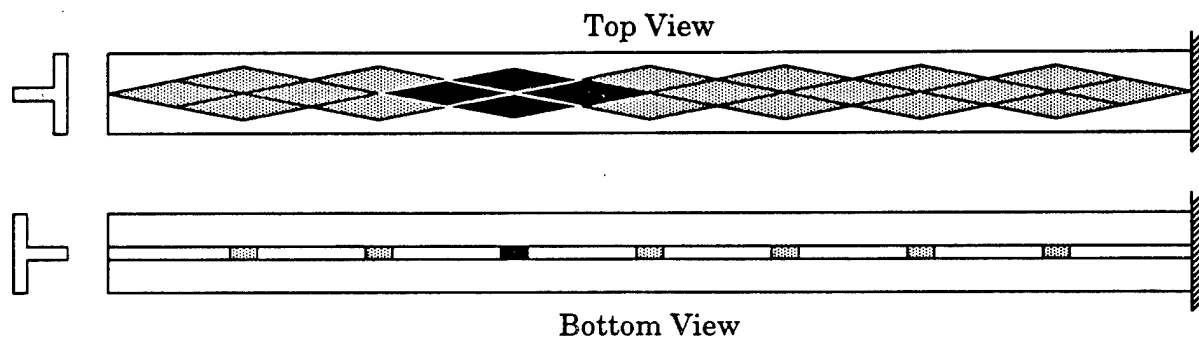


**Figure 6.2:** T-Section beam with arrangement of array of 22 Bartlett sensors on the top surface and seven point sensors on the bottom surface of the central flange.

length, or 3.75 inches long. The arrangement of sensors is shown in Figure 6.1. In Figure 6.2 are shown the Bartlett sensors on the top face as well as the seven rectangular PVDF patches, each 1/2 inch long, designed to simulate point sensor measurements. These point sensors are distributed at regular intervals along the bottom face of the central flange.

The arrangement of Bartlett sensors was designed so that the outputs of four neighboring sensors could be added together to simulate the output of a Bartlett sensor of twice the size. Each large sensor had a length of 7.5 inches, and overlap

with the adjacent sensors over half its length. For example, the sensors shaded in black in Figure 6.2 show one such large sensor. Using 22 smaller Bartlett sensors, a total of seven large sensors can be formed. The seven point sensors mounted on the bottom face of the flange are aligned with the centers of the seven large Bartlett sensors as shown in Figure 6.2.

The beam was mounted in a cantilever configuration, and a Brüel & Kjær electromagnetic shaker was attached to the bottom side of the central flange at the tip of the beam using a thin stinger. A white noise force was applied to the beam using the shaker, and the transfer functions from this tip force to the outputs of all 22 Bartlett sensors and seven point sensors were obtained. In addition, a non-contacting displacement sensor was mounted at the tip of the beam to measure the displacement of the top flange of the beam. All the transfer functions were measured in three frequency ranges, from 2 Hz to 20 KHz.

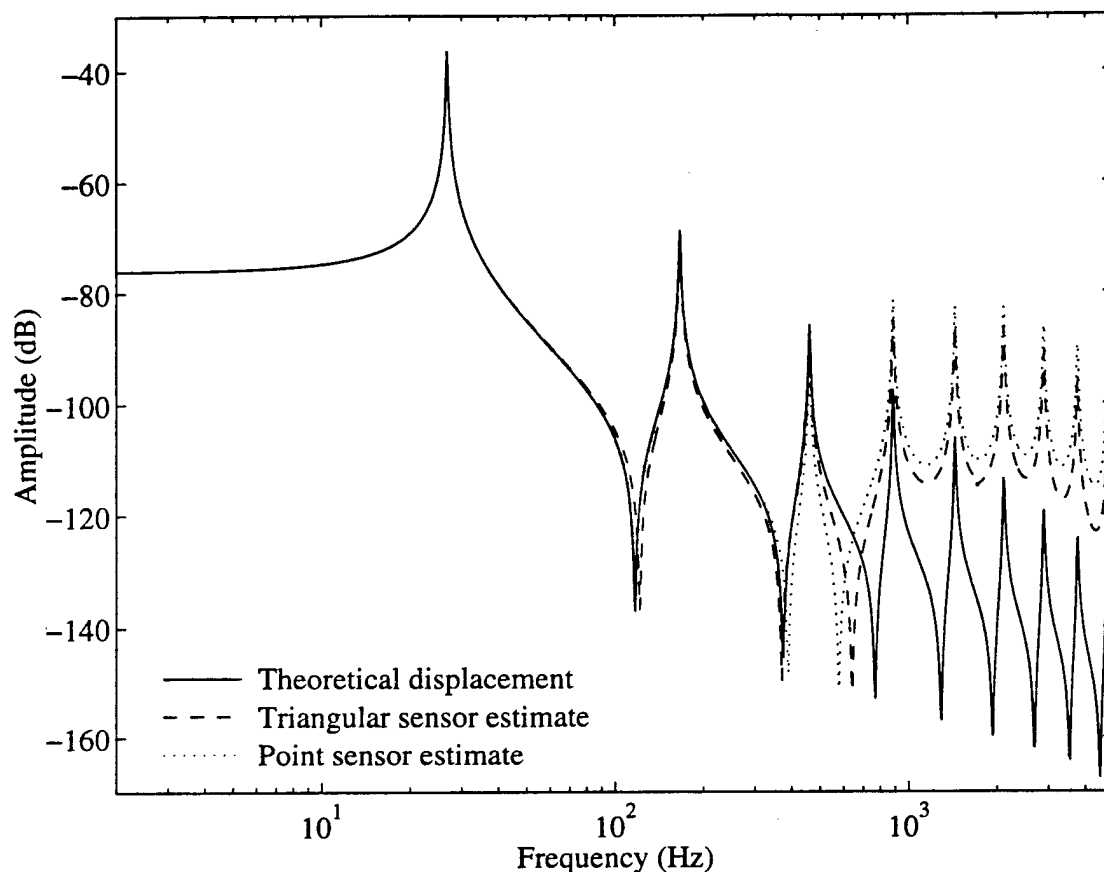
To compare with the experimental results, a finite element model of the beam was constructed using eight-node solid elements. A dynamic model was created which allowed simulated transfer functions from tip force to Bartlett and point sensor outputs to be computed.

A number of spatial integration schemes were employed in order to estimate displacement. It is assumed that the strain sensor outputs distributed along the length of the beam is proportional to the beam curvature,  $\partial^2 w(x)/\partial x^2$ . Spatial integration can then be performed twice to obtain an estimate of beam displacement,  $w(x)$ . Two simple integration schemes used were the trapezoidal scheme and Simpson's rule. For each of these schemes, the curvature at the tip of the beam was assumed to be zero. Unfortunately, no root sensor was etched on the PVDF and the root curvature had to be estimated by linearly extrapolating the measurements of the two sensors closest to

the root. Two more shape estimation schemes were considered. These were the GDSF scheme, where the curvature profiles of the first seven bending modes were fit to the sensor measurements, and the LSGDSF-4 scheme, where the curvatures of the first four bending modes were fit to the seven sensor measurements. The outputs of both the large Bartlett sensors and the point sensors were used to estimate tip displacement, in order to verify the beneficial effects of using shaped sensor measurements in structural shape estimation, rather than point sensor measurements.

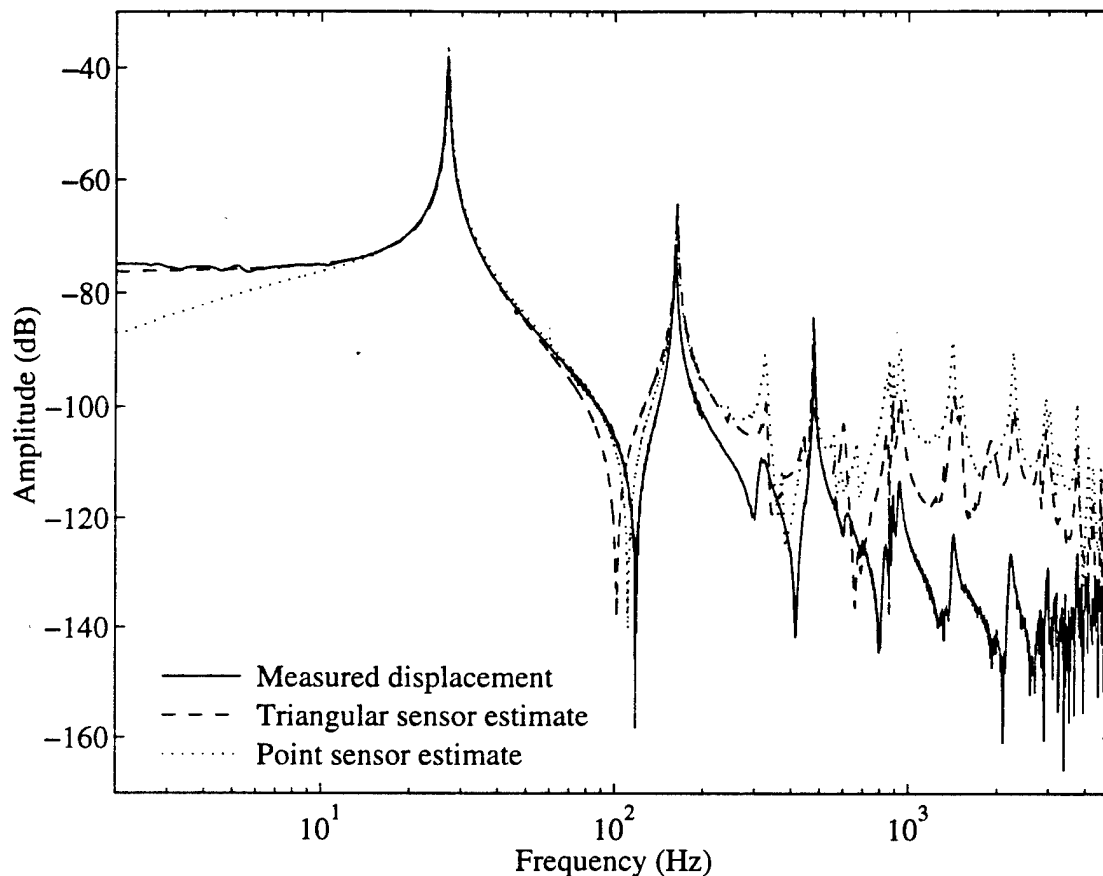
## 6.2 Trapezoidal Rule

Figure 6.3 compares transfer functions obtained using a finite element model of the beam. The solid line shows the transfer function from tip force to collocated tip displacement, which rolls off asymptotically at  $-30$  dB/decade in temporal frequency, and possesses the familiar alternating pole-zero pattern. The dashed and dotted curves were obtained by numerically integrating the analytical transfer functions from tip force to Bartlett and point strain sensor outputs, respectively, using the trapezoidal scheme. Good correspondence between estimated response and analytical transfer functions is seen up to the third mode of the beam. Beyond the third mode spatial aliasing occurs, and the seven distributed sensors are incapable of distinguishing modeshapes of higher spatial frequency than the third mode. The estimated tip displacement is generally larger than expected, and there is a loss of many zeros in the estimated response. It can be seen that the Bartlett sensors yield tip displacement estimated which are at least 5 dB less than those found using point sensors, indicating that some rolloff in the shaped sensor magnitude has taken place and that higher order modes are less observable. It will be seen that use of Simpson's rule to perform the numerical integration yielded results very similar to those obtained with the trapezoidal rule.



**Figure 6.3:** Comparison of transfer functions of a finite element model, from tip force to exact tip displacement and tip displacement response estimated from simulated sensor outputs using the trapezoidal rule.

Figure 6.4 compares the measured transfer function from tip force to tip displacement with the estimates of this response using Bartlett and point sensor data. The trapezoidal estimation procedure was carried out in the same manner as for the finite element model predictions, and shows that good estimates are available up to the third mode of the beam. Beyond this point aliasing again occurs and larger displacements are predicted, some  $180^\circ$  out of phase with the actual measurements. As with the finite element model results, the modes above the third are still visible in the estimated response, and the estimation errors observed using the Bartlett sensors is at least 10 dB lower than those for the point sensors.



**Figure 6.4:** Comparison of experimentally measured transfer functions from tip force to actual tip displacement and tip displacement response estimated by numerically integrating measured sensor transfer functions using the trapezoidal rule.

### 6.3 Simpson's Rule

Shown in Figure 6.5 is a comparison of the estimated tip displacement response using Simpson's rule to integrate the sensor measurements for the finite element model of the beam. Very little difference between the performance of Simpson's rule and the trapezoidal rule is seen: Simpson's rule estimates the first three modes and first two zeros accurately and then is subject to the problems associated with spatial aliasing of the higher modes. As with the trapezoidal rule, the errors obtained using the

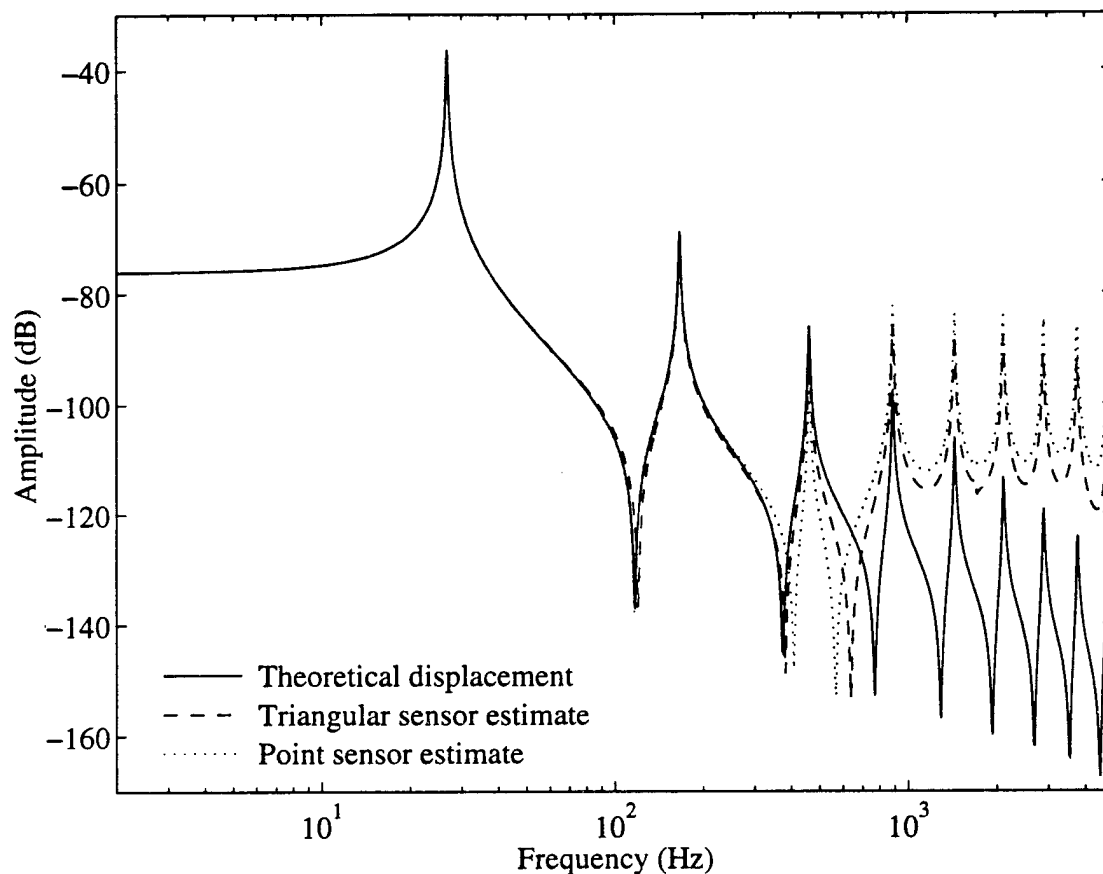


**Figure 6.5:** Comparison of transfer functions of a finite element model, from tip force to exact tip displacement and tip displacement response estimated from simulated sensor outputs using Simpson's rule.

triangular sensors are lower than those found with the point sensors.

Figure 6.6 shows a comparison of experimentally measured and estimated tip displacement response using Simpson's rule. Since little difference is seen between the estimation performance of the trapezoidal and Simpson's rules when using the finite element model results, it follows that very little difference would be seen when using measured data. This is indeed the case, and we see reasonable agreement between experiment and theory up the third mode, ignoring the presence of the torsion mode which should ideally be unobservable. Beyond the third mode we have larger and



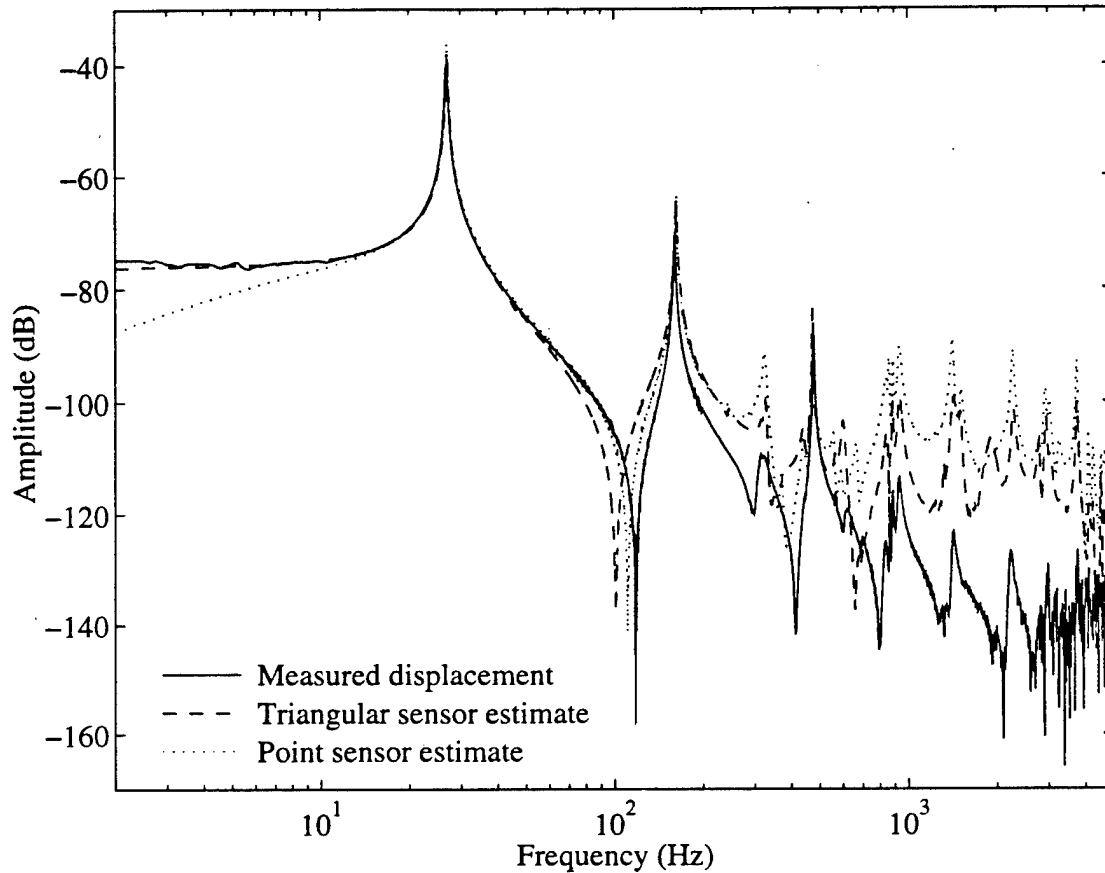


**Figure 6.6:** Comparison of experimentally measured transfer functions from tip force to actual tip displacement and tip displacement response estimated by numerically integrating measured sensor transfer functions using Simpson's rule.

larger estimation errors, although the point sensor estimates are consistently larger than the triangular sensor estimates.

## 6.4 GDSF Scheme

Figure 6.7 is a comparison of theoretical estimation performance when using the global dynamic shape function fitting scheme using as many shapes as point or triangular sensor measurements. It is found that the performance of the GDSF scheme

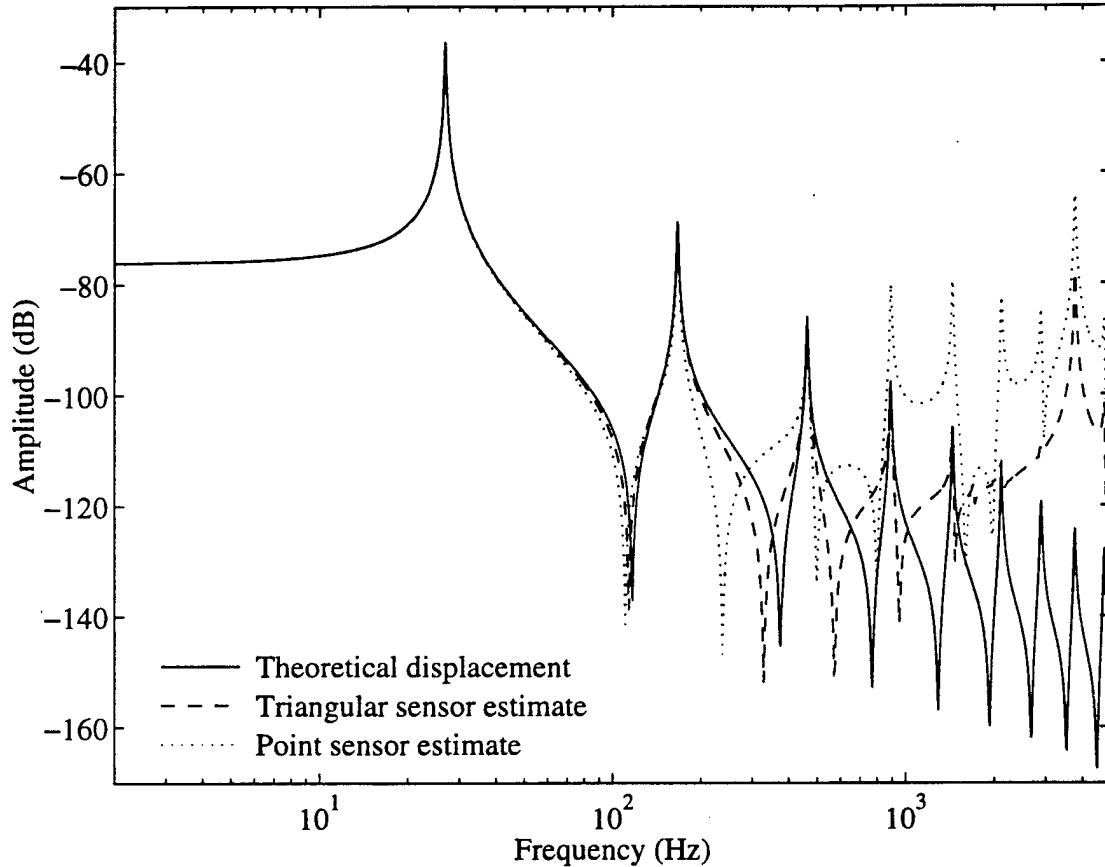


**Figure 6.7:** Comparison of transfer functions of a finite element model, from tip force to exact tip displacement and tip displacement response estimated from simulated sensor outputs using the GDSF scheme.

is severely limited due to the lack of a root sensor measurement. This is evident in the behavior of the estimates beyond the third mode of the beam. The second zero is actually badly estimated, and beyond the third mode significant errors are introduced, mainly through spatial aliasing. We see somewhat better behavior when using triangular sensors, as the errors are always lower than those obtained using point sensor measurements.

The estimation performance of the GDSF scheme when using experimental data is summarized in Figure 6.8. We see significant problems when using point sensor

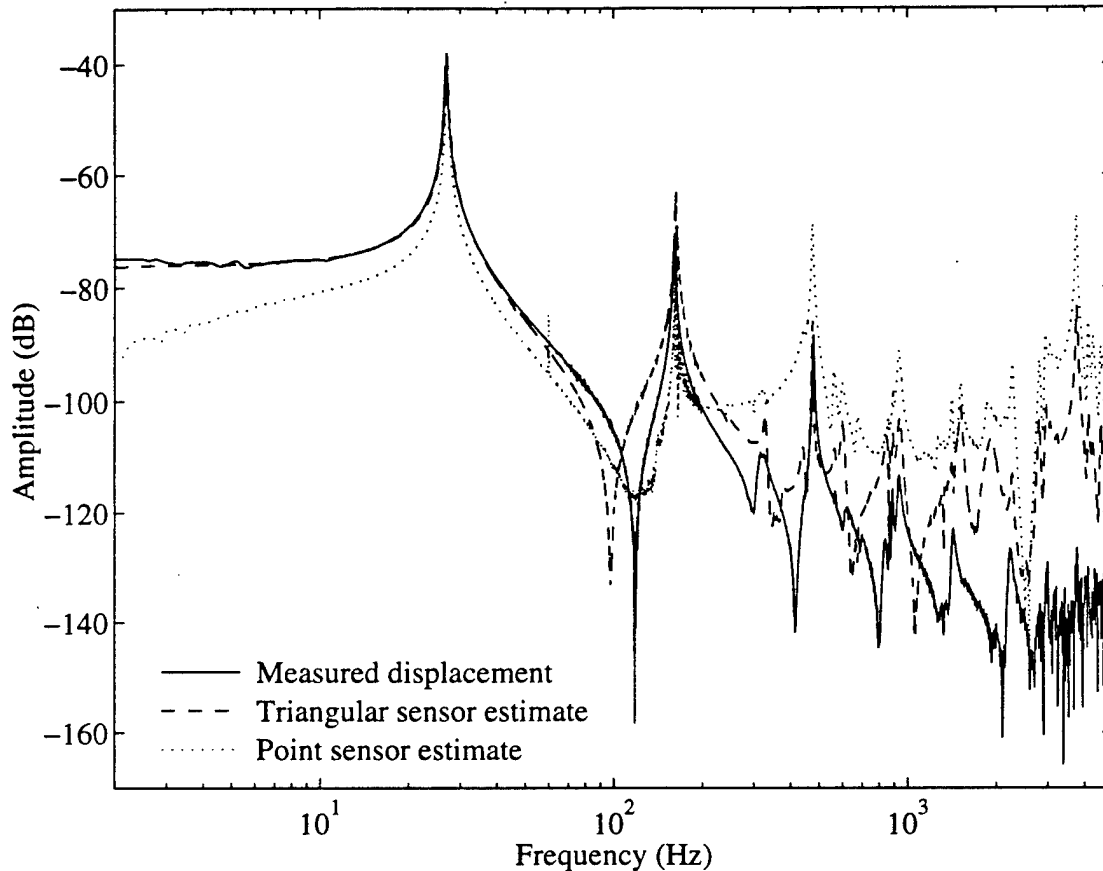


**Figure 6.8:** Comparison of experimentally measured transfer functions from tip force to actual tip displacement and tip displacement response estimated by numerically integrating measured sensor transfer functions using the GDSF scheme.

measurements. Indeed, there are magnitude errors at the lower frequencies and the first zero is very badly resolved and appears quite damped. In contrast the triangular sensor estimates perform much better in terms of magnitude estimation, although there is a large error in the estimate of the first zero frequency. The point sensors appear to predict the second mode resonance reasonably well but perform poorly in the estimation of the third mode. Beyond, errors are consistently large, indicating aliasing of the higher modes. The triangular sensors offer a better estimate of the third mode, and display smaller errors than the point sensors.

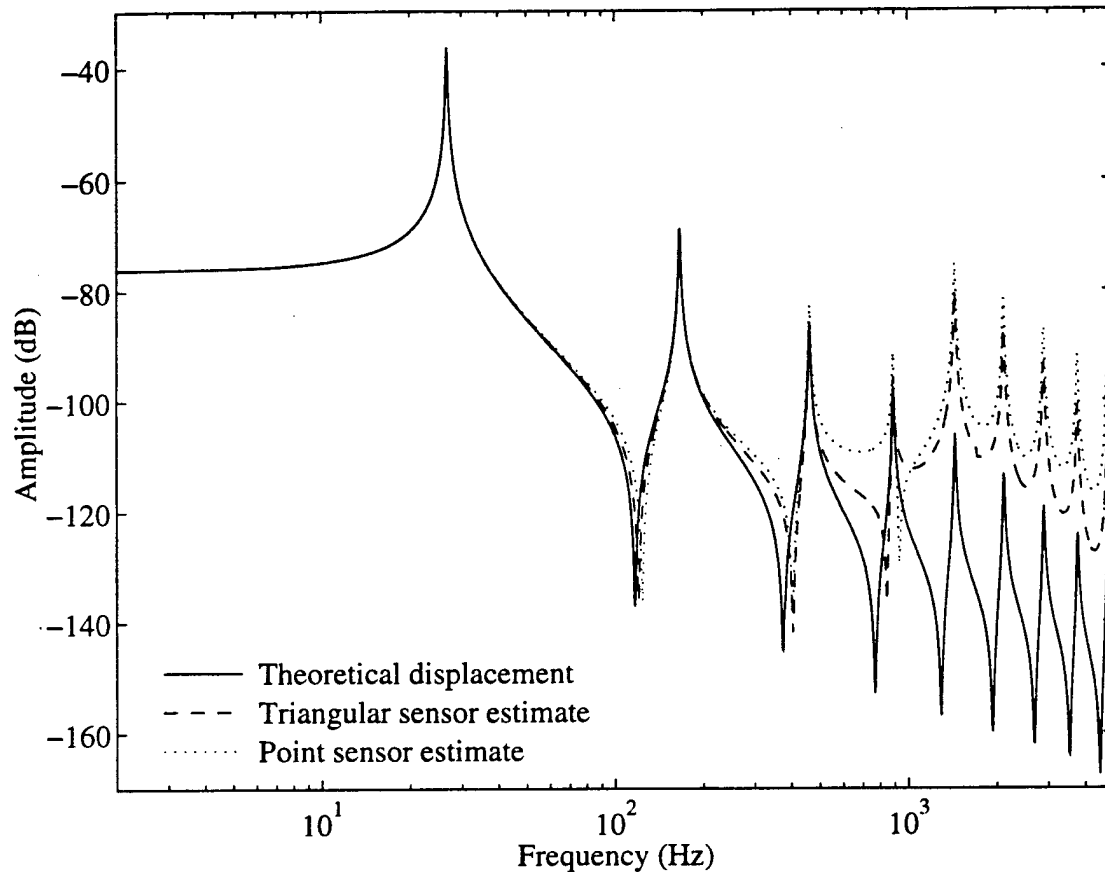


**Figure 6.9:** Comparison of transfer functions of a finite element model, from tip force to exact tip displacement and tip displacement response estimated from simulated sensor outputs using the LSGDSF-4 rule.

## 6.5 LSGDSF Scheme

Figure 6.9 compares the analytical and estimated response from tip force to tip displacement using the LSGDSF-4 fitting scheme with a finite element model. It can again be seen that good estimation is obtained up to the third mode of the beam. For the fourth mode, the tip displacement is underpredicted by the LSGDSF-4 scheme as the mode is barely visible. Beyond the fourth mode, spatial aliasing is observed and tip displacements are overpredicted. The asymptotic rolloff of the estimated response is consistent with the actual transfer function, and the estimated response

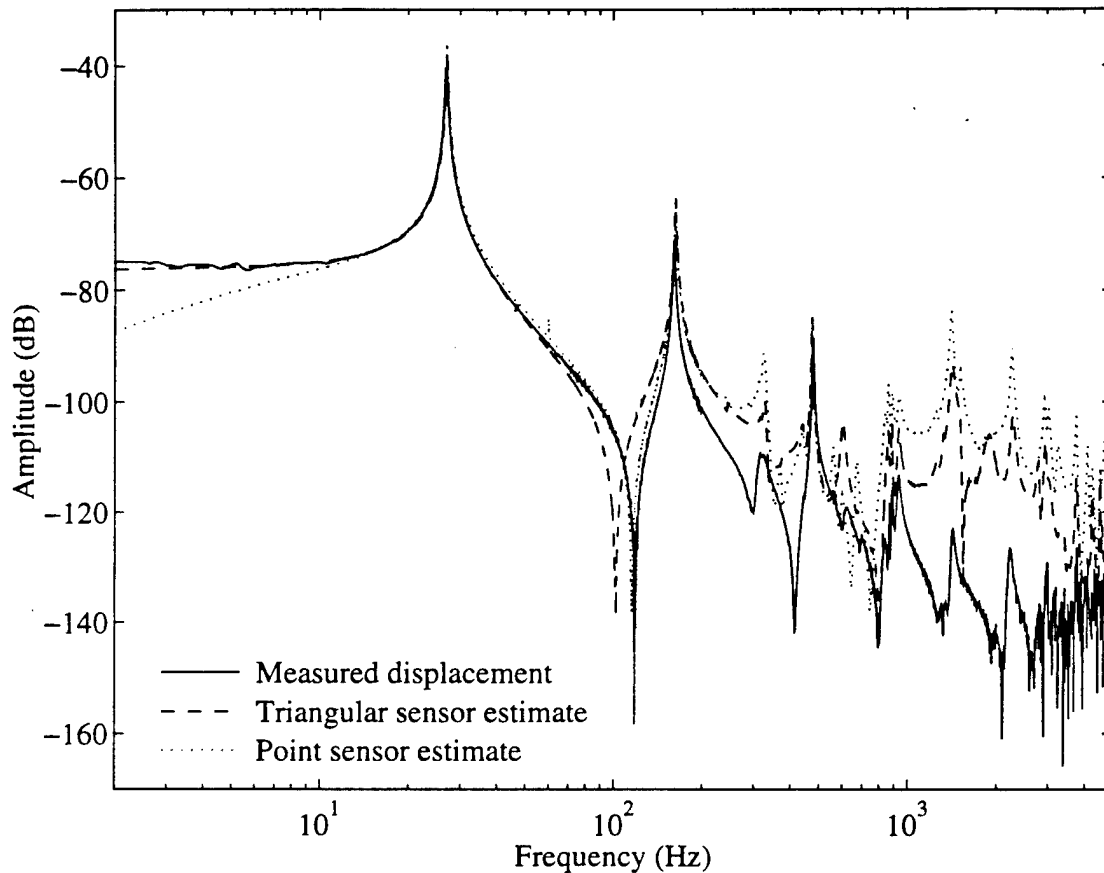


**Figure 6.10:** Comparison of experimentally measured transfer functions from tip force to actual tip displacement and tip displacement response estimated by numerically integrating measured sensor transfer functions using the LSGDSF-4 rule.

using Bartlett sensor data offers smaller errors than that for the point sensors.

Figure 6.10 compares the measured and estimated tip displacement response to tip for disturbance, when using the LSGDSF-4 scheme. Once again good estimation is available up to the third mode, with aliasing deteriorating results at higher frequency. The residue of the third mode is slightly more accurately estimated using the LSGDSF-4 scheme than with the trapezoidal rule. For higher frequencies, although estimates are much larger than in reality, the peaks of the modes appear in

the response estimate.

Interestingly, adding more shape functions to the estimation scheme is not necessarily beneficial. When examining the results of the GDSF scheme, which uses the first seven modeshapes, it was seen that the aliasing problems at the eight mode and above actually yield much larger errors than when using the LSGDSF scheme using four mode shapes. This occurs when using the simulated transfer functions of a finite element model as well as when using the measured transfer functions of the sensors. This is largely due to the lack of a root sensor measurement which heavily degrades the performance of all the estimation methods, especially the GDSF scheme.

## 6.6 Summary

In summary, it is clear that good shape estimation can indeed be performed for low order modes using distributed strain measurements, as the first and second bending modes are well-estimated. From the finite element models, we expect that the first zero in the estimated response will have a higher frequency than the measured response for the trapezoidal and LSGDSF-4 schemes. Looking at the responses estimated from measured data it can be seen that the first zero in the estimate is actually lower than the measured zero for all the schemes and for both sensor types. Additionally, the second zero is not as well predicted as the finite element model suggests it could be. Although the measured tip displacement transfer function matches the modeled response quite well, it was seen that there was sometimes poor agreement in the modeled and measured zero frequencies for the individual sensors. It is probable that manufacturing errors and problems with the continuity of the PVDF electrode led to significant modeling errors for some sensors, leading to an adverse impact on estimation performance at higher frequencies.

## CHAPTER 7

---

# Conclusions

---

It has been shown that discrete spatially averaging strain sensors satisfy the functional requirements for distributed sensing for intelligent structures. Specifically, it is seen that triangular sensors provide good wavenumber characteristics while satisfying the functional requirements for discrete strain sensors. It possesses a good rolloff rate, its transfer function is positive for all wave numbers, it is finite in spatial extent and very easy to manufacture. These properties make it an ideal spatially averaging sensor.

It has also been shown that care must be exercised in the design and implementation of sensors which need to be truncated at boundaries of the structure. The more derivatives are zero at the boundary, the better the sensor rolloff, and the closer its performance comes to that of an untruncated sensor. However, since this reduces the effective length of the sensor, the rolloff frequency will increase.

For the estimation of global dynamic beam modeshapes, it was seen that good results could be obtained when estimating the modeshapes of the pinned-pinned beam by using sensors with good rolloff rates. This was made possible to a large extent by the length of the sensors, which decreased the rolloff frequency. It was also seen that the rolloff afforded by the triangular sensors is crucial in keeping the error bounded for

higher modes. When using the point sensors, this error increases dramatically with wavenumber. It was also seen that it was difficult to correctly estimate the tip slope at frequencies below the first mode, due to the fact that the dynamic modeshapes cannot be used to form an accurate representation of the static displacement. This in turn is responsible for some of the problems seen in estimating the frequencies of the low order zeros.

For the clamped-free beam, we see much better performance at low frequencies and better estimation of the zeros. When using any integration scheme, it was found that a measurement at or localized near the root of the beam is crucial in minimizing the effects of spatial aliasing beyond about mode 7 or 8. It was found that with the trapezoidal and Simpson's schemes, that when no root measurement is available, some form of extrapolation of the root curvature using a linear or higher order scheme does not work well over a large range of frequencies, and a truly independent root measurement is best. It was found that a root measurement greatly improved the performance of the GDSF and LSGDSF schemes, especially beyond the mode corresponding to the number of shape functions used. In this region the errors are highly reduced by adding the root sensor and by using triangular sensors whose outputs are rolling off at these frequencies.

From the experimental results of shape estimation, it is seen that with the trapezoidal scheme, acceptable estimation performance was obtained up to about the third mode. Spatial aliasing degrades performance beyond this point, but it is clear that the errors in estimation observed using the triangular sensors is at least 10 dB lower than those for the point sensors. Results using the LSGDSF-4 and trapezoidal integration schemes are similar, although a slightly better estimate of the residue of the third mode is available with the LSGDSF-4 scheme.



It has been shown through simulations and experimental results that good shape estimation can be performed for low order modes using distributed strain measurements. It is clear from the experimental results that the frequencies of poles in the force to displacement transfer function are much easier to estimate than the zeros. This could be due to manufacturing errors which led to unmodeled behavior in some of the individual sensors.

---

## References

---

- [1] Andersson, M. S. and Crawley, E. F., "Discrete Distributed Strain Sensing of Intelligent Structures," *Proceedings, Second Joint Japan/U.S. Conference on Adaptive Structures*, Nagoya, Japan, November 12-14 1991, pp. 737-754.
- [2] Andersson, M. S. and Crawley, E. F., "Discrete Shaped Strain Sensors for Intelligent Structures," *Proceedings, 33rd AIAA/ASME/ASCE/AHS Structures, Structural Dynamics, and Materials Conference*, Dallas, TX, April 13-15 1992, pp. 566-576. AIAA paper No. 92-2046.
- [3] Burke, S. E., "Distributed Transducer Shading: Application to Structural Control, Hydrodynamics and Sonar Sensing," *Proceedings, Proceedings of the SPIE Conference on Smart Structures and Intelligent Systems*, Albuquerque, NM, Feb. 1993.
- [4] Burke, S. E. and Hubbard, J. E., "Distributed Actuator Control Design for Flexible Beams," *Automatica*, Vol. 24, No. 5, 1988, pp. 619-627.
- [5] Burke, S. E., Hubbard, J. E. J., and Meyer, J. E., "Colocation: Design Constraints for Distributed and Discrete Transducers," *Proceedings, 13th Biennial Conference on Mechanical Vibration and Noise*, Miami, Florida, September 22-25 1991, pp. 75-81. DE Vol. 34.
- [6] Collins, S. A., Padilla, C. E., Schmitz, E., Notestine, R. J., Ramey, M., and von Flotow, A. H., "Design, Manufacture and Application to Space Robotics of Distributed Piezoelectric Film Sensors," *Proceedings, 31st*

- AIAA/ASME/ASCE/AHS/ASC Structures, Structural Dynamics, and Materials Conference*, Long Beach, CA, April 2-4 1990, pp. 1899-1906.
- [7] Jacques, R. N. and Miller, D. W., "Multivariable Model Identification from Frequency Response Data," in *Proceedings of the 32nd Conference on Decision and Control*, 1993.
- [8] Kashiwase, T., Tabata, M., Tsuchiya, K., and Akishita, S., "Shape Control of Flexible Structures," *Journal of Intelligent Material Systems and Structures*, Vol. 2, Jan. 1991, pp. 110-125.
- [9] Lee, C. K., "Theory of Laminated Piezoelectric Plates for the Design of Distributed Sensors/Actuators. Part I: Governing Equations and Reciprocal Relationships," *The Journal of the Acoustical Society of America*, Vol. 87, No. 3, Mar. 1990, pp. 1144-1158.
- [10] Lee, C. K., Chiang, W. W., and O'Sullivan, T. C., "Piezoelectric Modal Sensors and Actuators Achieving Critical Damping on a Cantilever Plate," *Proceedings, 30th AIAA/ASME/ASCE/AHS Structures, Structural Dynamics, and Materials Conference*, Mobile, AL, April 3-5 1989, pp. 2018-2026.
- [11] Lee, C. K. and Moon, F. C., "Laminated Piezopolymer Plates for Torsion and Bending Sensors and Actuators," *The Journal of the Acoustical Society of America*, Vol. 85, No. 6, June 1989, pp. 2432-2439.
- [12] Lee, C. K. and Moon, F. C., "Modal Sensors/Actuators," *Journal of Applied Mechanics*, Vol. 57, 1990, pp. 434-441.
- [13] Sullivan, J. M., Hubbard, Jr., J. E., and Burke, S. E., "Modeling Approach for Two-Dimensional Distributed Transducers of Arbitrary Spatial Distribution,"

*Proceedings, Proceedings of the SPIE Conference on Smart Structures and Intelligent Systems*, Albuquerque, NM, Feb. 1993.

- [14] Wada, B. K., Fanson, J. L., and Crawley, E. F., "Adaptive Structures," *Journal of Intelligent Material Systems and Structures*, Vol. 1, No. 2, 1990, pp. 157-174.

AIR FORCE OF SCIENTIFIC RESEARCH (AFSC)

NOTICE IS HEREBY GIVEN THAT THE FOLLOWING INFORMATION IS  
CLASSIFIED "SECRET" AND IS TO BE CONTAINED IN  
AFSC 190-12

Approved for public release,  
distribution unlimited